

Harnessing physical entropy noise in structurally metastable 1T' molybdenum ditelluride for true random number generation

Yang Liu^{1,2}, Pengyu Liu¹, Yingyi Wen¹, Zihan Liang³, Songwei Liu¹, Lekai Song¹, Jingfang Pei¹, Xiaoyue Fan⁴, Teng Ma⁵, Gang Wang⁴, Shuo Gao⁶, Kong-Pang Pun¹, Xiaolong Chen³, Guohua Hu^{1,*}

¹Department of Electronic Engineering, The Chinese University of Hong Kong, Shatin, N. T., Hong Kong S. A. R., China

²Shun Hing Institute of Advanced Engineering, The Chinese University of Hong Kong, Shatin, N. T., Hong Kong S. A. R., China

³Department of Electrical and Electronic Engineering, Southern University of Science and Technology, Shenzhen, 518055, China

⁴School of Physics, Beijing Institute of Technology, Haidian, Beijing, 100081, China

⁵Department of Applied Physics, Hong Kong Polytechnic University, Hung Hom, Kowloon, Hong Kong S. A. R., China

⁶School of Instrumentation and Optoelectronic Engineering, Beihang University, Beijing, 100191, China

*Correspondence to: ghhu@ee.cuhk.edu.hk

KEYWORDS: True random numbers, molybdenum ditelluride, ferroelectric polarization, physical entropy noise, cryptography.

ABSTRACT: True random numbers are essential in various research and engineering problems. Their generation depends upon a robust physical entropy noise. Here, we present true random number generation by harnessing the conductance noise probed in structurally metastable 1T' molybdenum ditelluride (MoTe₂). The noise, well-fitting a Poisson process, is proved a robust physical entropy noise at low and even cryogenic temperatures. Noise characteristic analysis suggests the noise may originate from the polarization variations of the underlying ferroelectric dipoles in 1T' MoTe₂. We demonstrate the noise allows for true random number generation, enabling their use as seed for generating high-throughput secure random numbers exceeding 1 Mbit/s, appealing for practical applications in, for instance, cryptography where data security is now a severe issue. As an example, we show biometric information safeguarding in neural networks by using the random numbers as mask, proving a promising data security measure in big data and artificial intelligence.

Random numbers, a string of random bits, play a crucial role in research and engineering, for example, serving as the random input in numerical simulations and modeling, and introducing uncertainty in gaming and decision-making. ¹ However, the random numbers generated by deterministic algorithms are essentially pseudo-random. ² As the demand for randomness is increasingly stringent, the need for true random numbers has become critical. ³ Physical entropy noise with inherent true randomness, such as thermal noise from thermally agitated charges and 1/f noise from charge trapping dynamics in semiconductors, can be employed for deriving true random numbers. ⁴ However, arising from their physical nature, these physical entropy noises can be vulnerable to ambient noise and cryogenic attacks, undermining their reliability for true random number generation. ⁵

Nanomaterials with a plethora of quantum phenomena present promising solutions. ⁶⁻⁸ Amongst them, two-dimensional (2D) materials hold great interest, given their low-dimensionality and the quantum confinements, and the exhibited random variations in their underlying (opto)electronic and photonic processes. ^{9,10} They can also give flexible integration and synergy with modern electronics. ^{11,12} Indeed, reports show the random dynamics in emerging 2D materials and devices can be employed as robust physical entropy noises for true random number generators (TRNGs) and physically unclonable functions (PUFs) towards data and hardware cryptography. ¹³⁻¹⁸ 2D materials may even exhibit structural random variations. For example, molybdenum ditelluride (MoTe₂), a transition metal dichalcogenide, can exist in a prismatic-orthorhombic (2H-1T) intermediate octahedral 1T' phase. ¹⁹ The intermediate phase can induce metastable polarization of the underlying ferroelectric dipoles and, as a result, random variations in the electronic structures and properties. ²⁰ Studies show the structural metastability, intrinsic to the 1T' phase, is

even resilient to ambient noise and cryogenic attacks,^{21,22} manifesting the potential of using 1T' MoTe₂ for true random number generation.

In this work, we report true random number generation from electrochemical-exfoliated 1T' MoTe₂. We show the 1T' MoTe₂ allows stable conductance noise probing and, notably, fitting a Poisson process, the noise is proved a robust physical entropy noise even at low temperatures down to 15 K. Noise characteristic analysis, including spectral density and statistical time-lag, suggests the noise arises from the polarization variations of the underlying ferroelectric dipoles in 1T' MoTe₂. Using the noise, we realize true random number generation, and prove high-throughput secure random numbers exceeding 1 Mbit/s, appealing for practical applications, such as cryptography. Here we show safeguarding neural networks by masking key biometric information with the random numbers, proving a promising data security measure for big data and artificial intelligence.

Conductance noise probing: MoTe₂ predominantly exists in a stable 2H phase (Fig. 1a).²³ The 2H phase, however, can have local lattice distortions along the *y*-axis, with the Te atoms forming an octahedral coordination around the Mo atoms, leading to phase transition to a structurally metastable 2H-1T octahedral ferroelectric 1T' phase.^{23,24} 1T' MoTe₂ can be produced via physical and chemical engineering processes.^{25,26} Towards scalable applications, here we adopt the electrochemical exfoliation method (Fig. 1b; Supplementary Note 1).²⁷ Briefly, tetrahexylammonium cations intercalate the bulk MoTe₂, leading to exfoliation and distortion of the 2H structure. Figure 1c presents a solution of the exfoliated MoTe₂. Transmission electron microscopic (TEM) images of the nanosheets (Fig. 1d, e) show the MoTe₂ is successfully exfoliated with minimal defects. Particularly, a lattice spacing of 3.4Å and a non-hexagonal structure are revealed, indicating the exfoliated MoTe₂ is in the 1T' phase.²⁸ Electron diffraction

(Fig. 1e inset) shows a non-hexagonal rhombic, tetragonally symmetric lattice, confirming a 1T' phase. To verify the minimal defects, we perform X-ray photoelectron spectroscopic (XPS) analysis and prove a ~1:2 ratio for the Mo and Te atoms (Fig. S1). The minimal defects are ascribed to the tetrahexylammonium cation intercalation as the large molecules can effectively expand MoTe₂ while limiting the intercalations.²⁷ The minimal defects suggest the 1T' phase transition primarily arises from the intercalation-induced lattice distortion rather than defects.

The structural metastability in the 1T' phase may lead to random variations in the electrical properties. To probe the variations, we fabricate devices in a simple vertical structure, where the 1T' MoTe₂ is sandwiched between electrodes (Fig. S2; Supplementary Note 1). Indeed, as shown in Fig. 2a, the device shows resistance switching (switching ratio >10³) with random variations under sweeping bias, proving a randomly varying electrical conductivity of the 1T' MoTe₂. The switching on the other hand suggests a crystalline structure distortion towards the metallic 1T phase²⁶ and/or a potential Stark modulation of the conductivity.^{29,30} Nevertheless, the random variations may be harnessed as a physical entropy noise. For convenient operation, we measure the current output from the 1T' MoTe₂ devices under static bias instead of sweeping bias, and probe the random variations exhibited in the output.

We first study the output at 300 K and 0.05 V (Fig. 2b). See also Fig. S3a-h for the outputs at 0.1-5 V. As observed, stable variations are demonstrated in the outputs at all the bias conditions. For simplicity, we refer to the variations as conductance noise. We plot histograms of the outputs and fit Poisson process distributions, as shown in Fig. 2d (see also Fig. S3i-p). Note the outputs also conform to normal distributions (Fig. S4). Poisson process fitting is studied here to assess the randomness. A Poisson process describes a system of objects randomly distributed with an essential feature where the objects occur independently of one another.³¹ As such, the Poisson

process fitting proves the conductance noise is random, i.e. a physical entropy noise.³² Given the request of the true random number applications for sustaining cryogenic attacks, we extend our assessment to cryogenic temperatures (Fig. 2c). As shown, stable conductance noise is proved at all the low temperatures, and the outputs can fit Poisson processes (Fig. 2e-g). Here we note the Poisson fittings at the varying temperatures develop essentially consistent fitting characteristics, and that a larger λ at the higher temperatures means a larger averaged number of occurring events per interval only.³¹ Nevertheless, our investigation proves the conductance noise is a robust physical entropy noise stable even at cryogenic temperatures.

As discussed, noise from thermal and ambient electronics stands as a key source of physical entropy noise.⁴ We concurrently test ambient noise to study whether the conductance noise is due to the ambient noise from thermal and/or the electrical test set-ups. As shown in Fig. 2b, c, the ambient noise is smaller than the conductance noise by several orders of magnitude, proving the conductance noise is primarily from 1T' MoTe₂ rather than the ambient noise. We also test the device-to-device and batch-to-batch conductance noises (Fig. S5 and S6). From the tests, we learn that the device fabrication approach is reliable, with an acceptable yield in the initial trials (~70-80%), and that the measured conductance noises all can well fit Poisson processes, though the outputs may be different in the current values. Further materials and device engineering are required to improve the device fabrication yield and uniformity.

Origin of the conductance noise: To study the origin of the conductance noise, we perform current noise power spectral density (PSD) testing of the 1T' MoTe₂ devices at different bias and temperature conditions (Fig. 3a-d, Fig. S7). As shown, 1/f noise is proved over a broad frequency. For example, at 0.05 V, 300 K, the noise spectral power well fits 1, i.e. $\gamma \sim 1$, proving 1/f noise (Fig. 3c). However, as the frequency increases, the output may be flattened at low bias conditions,

indicating thermal noise dominates the high-frequency region (Fig. 3d). The flattening may be ascribed to the insufficient current signals at low bias conditions.^{33,34} Nevertheless, $1/f$ noise is proved for our $1T'$ MoTe_2 devices, suggesting charge fluctuations account for the conductance noise, for instance, charge trapping dynamics at the defect sites^{35,36} in our $1T'$ MoTe_2 . However, as observed, varying the bias and temperature does not really variate the $1/f$ noise, suggesting charge trapping by defects may not account for the conductance noise. Indeed, as discussed, our $1T'$ MoTe_2 have minimal defects. We therefore understand the conductance noise arises from the intrinsic property of $1T'$ MoTe_2 rather than the defects. Given the structural metastability of the ferroelectric $1T'$ phase, we assume the conductance noise is the reflection of the polarization variations of $1T'$ MoTe_2 . However, ferroelectric polarization (Fig. S8) and Raman spectroscopy (Fig. S9) characterizations show no deterministic collective, overall ferroelectric polarization. The collective polarization may have been compromised by the discrete nature of the exfoliated $1T'$ MoTe_2 nanosheets³⁷, and further characterizations on the individual nanosheets will be required to locate the exact polarization effect of the underlying ferroelectric dipoles. With the above investigations, we understand the conductance noise arises from the polarization variations of the ferroelectric dipoles in the individual $1T'$ MoTe_2 nanosheets rather than a collective polarization.

To investigate the origin further, we study the cumulative charge characteristic of the devices. Here we plot in Fig. 3e the output at 0.05 V, 300 K and the cumulative charge integrated during the sampling time intervals. The cumulative charge state can reflect the polarization state of the ferroelectric dipoles in $1T'$ MoTe_2 .³⁸ As observed, the cumulative charge proves a stable noise, indicating random variations in the polarization states. We adopt weighted time-lag, a method widely used to study noise characteristics,³⁹ to statistically evaluate this noise. Briefly, as plotted in Fig. 3f, the distribution of the cumulative charge is defined with a weighted time-lag, $TL =$

$lg \left(K \sum_n^{N-1} \frac{1}{2\pi\alpha^2} \exp \left(-\frac{[(Q_n-x)^2+(Q_{n+1}-y)^2]}{2\alpha^2} \right) \right)$, where Q_n and Q_{n+1} are the n -th and $(n+1)$ -th cumulative charge states, (x, y) denotes the corresponding TL plot coordinates, N is the total states, and α and K are the fitting parameters to ensure the TL maximum is 1 before logarithm. The cumulative charge states in the plot are distributed in ascending order, and a TL approaching 0 means a stronger correlation between the adjacent states. As observed, the TL plot shows random yet uniform aggregations with a bimodal distribution along the diagonal – both the larger and smaller cumulative charge states establish stronger correlations, while the medium cumulative charge states weaker correlations. This indicates the ferroelectric dipoles are uniformly distributed with bimodal aggregations, and that the strongly polarized dipoles may require a stronger current and a longer time to reverse.

See Fig. S10 for the control experiments on the ambient noise and a MoS_2 device, where we demonstrate the ambient noise and random telegraph noise develop distinctly different cumulative charge profiles and TL patterns. The comparison aligns with our understanding that the conductance noise arises from the polarization variations of the underlying ferroelectric dipoles in $1T'$ MoTe_2 .

We conduct Monte Carlo simulation on the polarization states of the ferroelectric dipoles in $1T'$ MoTe_2 (as illustrated in Fig. 3g). See Supplementary Note 2 for the simulation method. Based on our understanding, the ferroelectric dipoles are uniformly distributed and undergo polarization variations. Under a static bias, the polarization variations can lead to fluctuations of the bound charges and thus, the conductance noise. As studied by the Monte Carlo simulation, the output renders a stable noise, consistent with our experimental results (Fig. 3h); the conductance noise also well fits a Poisson process (Fig. 3i). Therefore, the Monte Carlo simulation from the

perspective of bound charge fluctuations aligns with our understanding that the conductance noise arises from the polarization variations of the ferroelectric dipoles.

True random number generation: We design a very simple circuit in Cadence Virtuoso to harness the conductance noise for true random number generation (Fig. 4a, b). The circuit consists of a 1T' MoTe₂ device, an I/V converter, a high pass filter, a voltage amplifier, and a comparator. Upon operation, the converter transforms the output from the 1T' MoTe₂ device into a voltage signal for convenient signal processing. The voltage signal, i.e. '*Output 1*' (Fig. 4c), demonstrates a noise that can well fit a Poisson process (Fig. 4d). This shows the circuit has well captured the conductance noise from the 1T' MoTe₂ device. The voltage signal then passes through the filter and amplifier to extract the noise in the form of differentiated voltage spikes, i.e. '*Output 2*' and '*Output 3*' (Fig. 4c). As demonstrated, the voltage spikes also fit a Poisson process (Fig. 4e, f), proving the extracted noise remains a robust physical entropy noise. The comparator then processes the voltage spikes to yield random numbers in the form of 0's and 1's binary strings, i.e. '*Output 4*' (Fig. 4c). See also Fig. S11 for a zoomed-in distribution of the 0's and 1's digits. As demonstrated, the random 0's and 1's digits render a ratio of $\sim 1:1$ (Fig. 4g), suggesting the numbers are random.

To verify the random numbers are truly random, we test the randomness using the National Institute of Standards and Technology (NIST) randomness testing suite that is widely used to evaluate the randomness.⁴⁰ As shown in Table S1, the random numbers successfully pass the test, proving their true randomness. However, the throughput is ~ 10 bit/s, limiting their use.

To address the limitation, employing a common approach in the field,⁴¹ we use the random numbers as seed and introduce them to a Non-Linear Feedback Shift Register (NLFSR; Fig. S12)

for high-throughput random number output with a rate of, say, 1 Mbit/s (Fig. 4a, b). Here, as a case example, we present in Fig. S13 a random number bitmap generated using the high-throughput random numbers. Notably, as shown in Table S2, the high-throughput random numbers also fully pass the NIST randomness test.

Here we note the electrical components (e.g. the resistors and comparators) in Fig. 4b are configured to adapt to room temperature operation. For low temperature (e.g. 15 K) operations, the electrical components need to be reconfigured to adapt to low current values, and special temperature-compensating and corrective circuits may be used.⁴² Nevertheless, the demonstrated capability of our 1T' MoTe₂ devices for surviving cryptogenic attacks is critical for TRNG applications, outperforming the current TRNG techniques (Table S3).

Safeguarding neural networks: High-throughput secure random numbers are appealing for practical applications.³ As an example, we apply the high-throughput secure random numbers in cryptography. Cryptography is of critical importance in the current age with the data exponentially growing and at the risk of being attacked and sabotaged.³ See Fig. S14 and S15 for demonstrations of password generation and data encryption.

Beyond the common cryptographic applications, the importance of cryptography is manifested by the rapid advances of neural networks. Neural networks are widely used in, for instance, image recognition, sensing, autonomous driving, and manufacturing, where sensitive data is constantly required. Particularly, in the context of big data and artificial intelligence, sensitive biometric information such as retinas, facial characteristics, and fingerprints is excessively used and potentially leaked.⁴³ Secure data protection has therefore become a critical issue, and adversarial attacks in neural networks pose a significant threat.⁴³ Here we adopt a differential safeguarding

strategy (Fig. S16) and investigate its effectiveness to obfuscate sensitive data in neural networks.

⁴³ The differential safeguarding framework injects random numbers as noise into the target data for perturbation. Following this approach, we train a residual neural network (ResNet) for pet recognition (Fig. 5a; Supplementary Note 3). ResNets are a widely used model for image and pattern recognition. ⁴⁴ After training, the model performs successful pet recognition with an accuracy of 92%. See the confusion matrix and performance of the well-trained model in Fig. S17.

We then inject the random numbers as noise into the target validation data. Interestingly, as shown in Fig. 5a, taking the image of a Siamese cat for demonstration, the noise perturbation appears negligible to human eyes. This is ascribed to the innate ability of the human brain to process visual information holistically, i.e. focusing on the broader picture rather than the minute details. ⁴⁵ However, as demonstrated in Fig. 5b, the noise perturbation substantially affects the recognition of the model at all the convolution layers. The confusion matrix and accuracy (~78%) demonstrate the ResNet variant with the noise perturbation gives a poor performance in recognition (Fig. 5c, d). See also Fig. S18 for the confusion matrix details with noise perturbation. Comparing the accuracies with and without the noise perturbation (Fig. 5d), a bit noise perturbation can cause a substantial degradation in the classification accuracy. This is because the noise disrupts the feature detection capability of the ResNet variant model in the initial layers, which then propagates to the deeper layers, leading to exacerbation of the errors. ⁴⁶ The detailed difference (i.e. Δ) between the two success rates in the different 37 categories can be found in Fig. 5e. The findings prove that injecting the random numbers as noise perturbations that are not discernible to eyes can substantially interfere with the neural networks and as such, enhance data security in neural networks.

In conclusion, we have reported true random number generation using structurally metastable 1T' MoTe₂. Our analysis suggests the polarization variations of the ferroelectric dipoles in 1T' MoTe₂ give rise to a conductance noise, and that the noise can be harnessed as a robust physical entropy noise for true random number generation. Notably, the noise remains stable even at cryogenic temperatures, critical for the cryogenic applications of true random numbers. We have proved true random number generation and their use as the seed for high-throughput secure random number generation exceeding 1 Mbit/s, appealing for various practical applications, for instance, cryptography. As an example, we demonstrate data safeguarding in neural networks by using the random numbers as the mask. Neural networks pose a significant threat to data security, particularly the biometric information, in big data and artificial intelligence by adversarial data leakage and attacks. Our safeguarding approach can serve as a critical data security measure. Given this, and the scalability as well as seamless integration possibility with the electronics systems of the electrochemical-exfoliated 1T' MoTe₂, our approach of true random number generation holds great potential to enable secure data in neural networks.

FIGURES

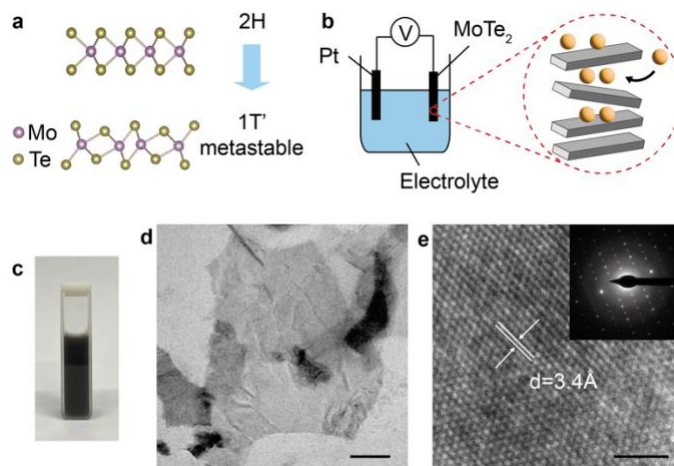


Figure 1. 1T' MoTe₂ by electrochemical exfoliation. (a) Crystalline structures of hexagonal 2H and distorted octahedral 1T' MoTe₂. (b) Schematic electrochemical exfoliation of MoTe₂, showing intercalation of molecular tetrahexylammonium cations between the MoTe₂ layers. Pt and MoTe₂ are used as the electrodes. (c) Dispersion of the exfoliated MoTe₂. (d, e) Transmission electron microscopic images and the selected electron diffraction pattern (inset of e) of the exfoliated MoTe₂ nanosheets, proving a distorted octahedral 1T' crystalline structure.

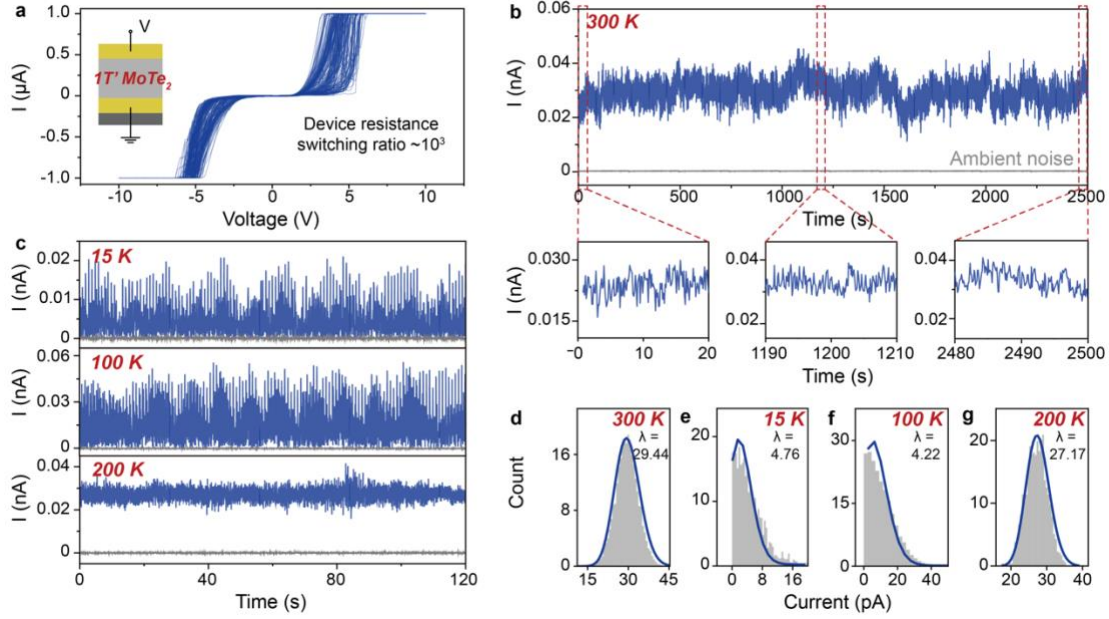


Figure 2. Conductance noise probing. (a) Current output for 100 sweeping test cycles of a typical 1T' MoTe₂ device, showing random variations in the device resistance switching at ~5 V. The switching ratio is estimated as 1424 between the averaged high and low resistances. The inset shows the device structure. (b) Current output from the device at 300 K, showing stable conductance noise probed from 1T' MoTe₂. (c) Current output at low temperatures, showing stable conductance noise. The bias is 0.05 V for all the tests. See Fig. S3 for the output at the other bias conditions. Ambient noise measured from suspended probing electrodes is presented in grey for comparison. (d-g) Histograms and Poisson fittings of the current output from (b) and (c), proving the conductance noise probed is a random process.

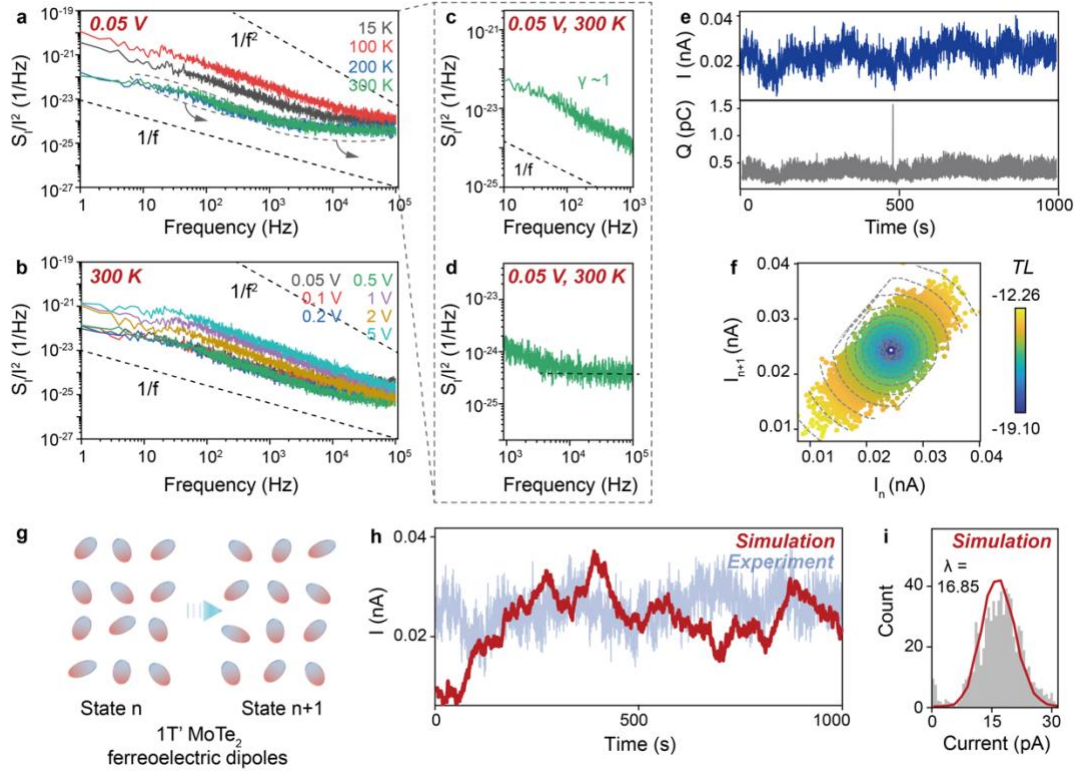


Figure 3. Origin of the conductance noise. Current power spectral density (PSD) of the 1T' MoTe₂ device at (a) 0.05 V and (b) 300 K, with (c, d) plotting PSD at low and high-frequency regions. PSD testing proves 1/f noise. (e) Current output and the corresponding cumulative charge fluctuation of the 1T' MoTe₂ device at 0.05 V, 300 K. The cumulative charge is integrated in the sampling interval of 0.067 s. (f) Time-lag plot for the cumulative charge fluctuation, showing bimodal distribution along the diagonal, suggesting stronger correlations for the larger and smaller cumulative charge states to the next states. (g) Varying n -th and $(n + 1)$ -th polarization states of the ferroelectric dipoles in 1T' MoTe₂ in our proposed conductance noise mechanism. (h) Current output from Monte Carlo simulation on polarization variations of the ferroelectric dipoles, with the current output in (e) plotted as the background for comparison. (i) Histogram and Poisson fitting of the current output from Monte Carlo simulation.

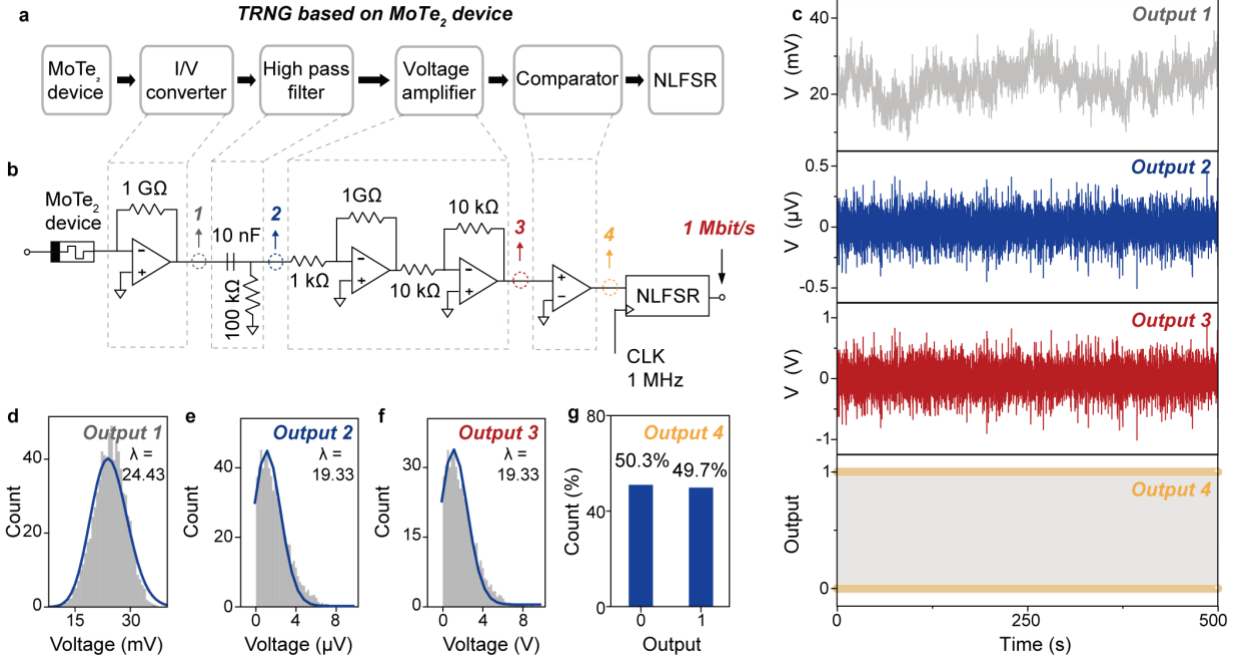


Figure 4. True random number generation. (a, b) Circuit design and diagram of the true random number generator (TRNG), consisting of the 1T' MoTe₂ device, I/V converter, high pass filter, voltage amplifier, comparator, and NLFSR. NLFSR (Fig. S12) is used to generate high-throughput random numbers from the seed, i.e. the true random numbers from Port 4. (c) The output obtained from the TRNG at Port 1-4, including the converted voltage output, the filtered voltage output, the amplified voltage output, and the generated true random numbers in a string of 0's and 1's. See Fig. S11 for the 0's and 1's string details. (d-f) Histograms and Poisson fittings of the data points from Output 1-3 in (c), proving all the outputs are random processes. Note absolute values are taken from the negative data points in Output 2 and 3 for the Poisson fittings. (g) Histogram of the 0's and 1's true random numbers in Output 4 in (c), demonstrating a ratio of $\sim 1:1$.

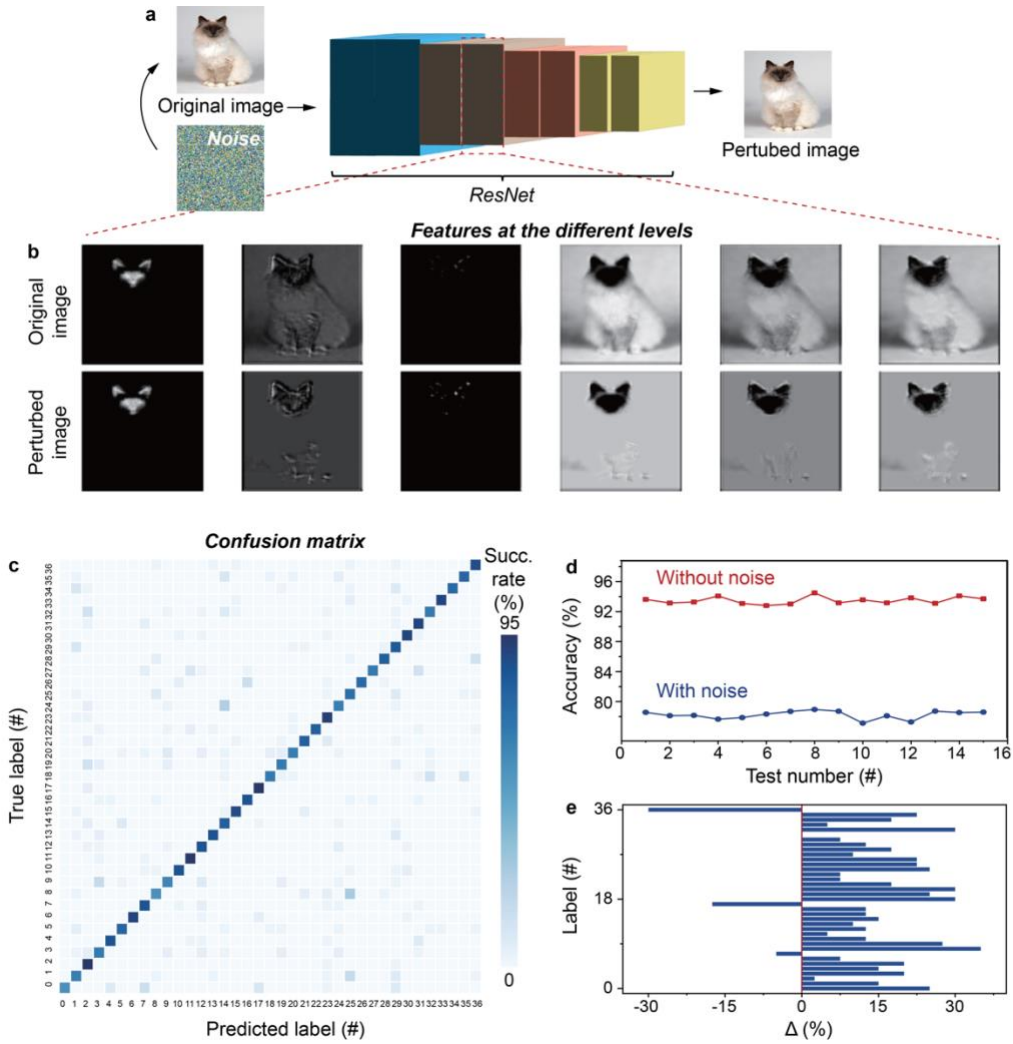


Figure 5. Safeguarding in neural networks. (a) ResNet variant architecture for cat recognition without and with noise perturbation. The noise map is produced using the high-throughput random numbers. (b) The cat images without and with noise perturbation at the intermediate convolution layers, showing the perturbed images lose certain features of the cat throughout the convolution layers. (c) Confusion matrix for the ResNet variant recognition with noise perturbation. The scale corresponds to the success rate of the predicted labels. The x and y coordinates denote the predicted and true labels of the 37 classifications in the training dataset. (d) The accuracy with and without noise perturbation at the different test numbers. (e) The difference between the success rates in the confusion matrices with and without noise perturbation along the diagonal. The x

coordinate denotes the difference in the success rate along the diagonal, and the y coordinate the 37 different classifications. The confusion matrix details with the success rate values are presented in Fig. S18.

Author Contributions

YL, GH designed the experiments. YL, PL, YW, ZL, SL, LS, JP, XF performed the experiments. YL, PL, GH analyzed the data. YL, GH prepared the figures. YL, GH wrote the manuscript. All authors discussed the results from the experiments and commented on the manuscript.

Funding Sources

GH acknowledges support from CUHK (4055115), YL from SHIAE (RNE-p3-21), JP and YW from RGC (24200521), TM from PolyU (P0042991), GW from NSFC (12074033), SG from National Key Research and Development Program of China (2023YFB3208003), XC from NSFC (62275117) and Shenzhen excellent youth program (RCYX20221008092900001).

REFERENCES

- (1) Stipčević, M.; Koç, Ç. K. True Random Number Generators. In *Open Problems in Mathematics and Computational Science*; Koç, Ç. K., Ed.; Springer International Publishing: Cham, 2014; pp. 275–315.
- (2) Gentle, J. E. *Random number generation and Monte Carlo methods*; Springer: New York, 2003.
- (3) Yu, F.; Li, L.; Tang, Q.; Cai, S.; Song, Y.; Xu, Q. A Survey on True Random Number Generators Based on Chaos. *Discrete Dyn. Nat. Soc.* **2019**, *2019* (1), 1–10.
- (4) Wali, A.; Das, S. Hardware and Information Security Primitives Based on 2D Materials and Devices. *Adv. Mater.* **2023**, *35* (18), 2205365.
- (5) Soucarros, M.; Clédière, J.; Dumas, C.; Elbaz-Vincent, P. Fault Analysis and Evaluation of a True Random Number Generator Embedded in a Processor. *J. Electron. Test.- Theory Appl.* **2013**, *29* (3), 367–381.
- (6) Abraham, N.; Watanabe, K.; Taniguchi, T.; Majumdar, K. A High-Quality Entropy Source Using van Der Waals Heterojunction for True Random Number Generation. *ACS Nano* **2022**, *16* (4), 5898–5908.
- (7) Kim, G.; In, J. H.; Kim, Y. S.; Rhee, H.; Park, W.; Song, H.; Park, J.; Kim, K. M. Self-Clocking Fast and Variation Tolerant True Random Number Generator Based on a Stochastic Mott Memristor. *Nat. Commun.* **2021**, *12* (1), 2906.
- (8) Liu, B.; Chang, Y.-F.; Li, J.; Liu, X.; Wang, L. A.; Verma, D.; Liang, H.; Zhu, H.; Zhao, Y.; Li, L.-J.; Hou, T.-H.; Lai, C.-S. Bi₂O₂Se-Based True Random Number Generator for Security Applications. *ACS Nano* **2022**, *16* (4), 6847–6857.

- (9) Wen, C.; Li, X.; Zanotti, T.; Puglisi, F. M.; Shi, Y.; Saiz, F.; Antidormi, A.; Roche, S.; Zheng, W.; Liang, X.; Hu, J.; Duhm, S.; Roldan, J. B.; Wu, T.; Chen, V.; Pop, E.; Garrido, B.; Zhu, K.; Hui, F.; Lanza, M. Advanced Data Encryption Using 2D Materials. *Adv. Mater.* **2021**, *33* (27), 2100185.
- (10) Glavin, N. R.; Rao, R.; Varshney, V.; Bianco, E.; Apte, A.; Roy, A.; Ringe, E.; Ajayan, P. M. Emerging Applications of Elemental 2D Materials. *Adv. Mater.* **2020**, *32* (7), 1904302.
- (11) Lanza, M.; Sebastian, A.; Lu, W. D.; Le Gallo, M.; Chang, M.-F.; Akinwande, D.; Puglisi, F. M.; Alshareef, H. N.; Liu, M.; Roldan, J. B. Memristive Technologies for Data Storage, Computation, Encryption, and Radio-Frequency Communication. *Science* **2022**, *376* (6597), eabj9979.
- (12) Lemme, M. C.; Akinwande, D.; Huyghebaert, C.; Stampfer, C. 2D Materials for Future Heterogeneous Electronics. *Nat. Commun.* **2022**, *13* (1), 1392.
- (13) Ghosh, S.; Zheng, Y.; Radhakrishnan, S. S.; Schranghamer, T. F.; Das, S. A Graphene-Based Straintronic Physically Unclonable Function. *Nano Lett.* **2023**, *23* (11), 5171–5179.
- (14) Ravichandran, H.; Sen, D.; Wali, A.; Schranghamer, T. F.; Trainor, N.; Redwing, J. M.; Ray, B.; Das, S. A Peripheral-Free True Random Number Generator Based on Integrated Circuits Enabled by Atomically Thin Two-Dimensional Materials. *ACS Nano* **2023**, *17* (17), 16817–16826.
- (15) Oberoi, A.; Dodda, A.; Liu, H.; Terrones, M.; Das, S. Secure Electronics Enabled by Atomically Thin and Photosensitive Two-Dimensional Memtransistors. *ACS Nano* **2021**, *15* (12), 19815–19827.

- (16) Wali, A.; Ravichandran, H.; Das, S. A Machine Learning Attack Resilient True Random Number Generator Based on Stochastic Programming of Atomically Thin Transistors. *ACS Nano* **2021**, *15* (11), 17804–17812.
- (17) Ravichandran, H.; Zheng, Y.; Schranghamer, T. F.; Trainor, N.; Redwing, J. M.; Das, S. A Monolithic Stochastic Computing Architecture for Energy Efficient Arithmetic. *Adv. Mater.* **2023**, *35* (2), 2206168.
- (18) Dodda, A.; Subbulakshmi Radhakrishnan, S.; Schranghamer, T. F.; Buzzell, D.; Sengupta, P.; Das, S. Graphene-Based Physically Unclonable Functions That Are Reconfigurable and Resilient to Machine Learning Attacks. *Nat. Electron.* **2021**, *4* (5), 364–374.
- (19) Lai, Z.; He, Q.; Tran, T. H.; Repaka, D. V. M.; Zhou, D.-D.; Sun, Y.; Xi, S.; Li, Y.; Chaturvedi, A.; Tan, C.; Chen, B.; Nam, G.-H.; Li, B.; Ling, C.; Zhai, W.; Shi, Z.; Hu, D.; Sharma, V.; Hu, Z.; Chen, Y.; Zhang, Z.; Yu, Y.; Renshaw Wang, X.; Ramanujan, R. V.; Ma, Y.; Hippalgaonkar, K.; Zhang, H. Metastable 1T'-Phase Group VIB Transition Metal Dichalcogenide Crystals. *Nat. Mater.* **2021**, *20* (8), 1113–1120.
- (20) Yuan, S.; Luo, X.; Chan, H. L.; Xiao, C.; Dai, Y.; Xie, M.; Hao, J. Room-Temperature Ferroelectricity in MoTe₂ down to the Atomic Monolayer Limit. *Nat. Commun.* **2019**, *10* (1), 1775.
- (21) Keum, D. H.; Cho, S.; Kim, J. H.; Choe, D.-H.; Sung, H.-J.; Kan, M.; Kang, H.; Hwang, J.-Y.; Kim, S. W.; Yang, H.; Chang, K. J.; Lee, Y. H. Bandgap Opening in Few-Layered Monoclinic MoTe₂. *Nat. Phys.* **2015**, *11* (6), 482–486.
- (22) Qi, Y.; Naumov, P. G.; Ali, M. N.; Rajamathi, C. R.; Schnelle, W.; Barkalov, O.; Hanfland, M.; Wu, S.-C.; Shekhar, C.; Sun, Y.; Süß, V.; Schmidt, M.; Schwarz, U.; Pippel, E.; Werner, P.; Hillebrand, R.; Förster, T.; Kampert, E.; Parkin, S.; Cava, R. J.; Felser, C.; Yan, B.;

- Medvedev, S. A. Superconductivity in Weyl Semimetal Candidate MoTe₂. *Nat. Commun.* **2016**, *7* (1), 11038.
- (23) Wang, Y.; Xiao, J.; Zhu, H.; Li, Y.; Alsaied, Y.; Fong, K. Y.; Zhou, Y.; Wang, S.; Shi, W.; Wang, Y.; Zettl, A.; Reed, E. J.; Zhang, X. Structural Phase Transition in Monolayer MoTe₂ Driven by Electrostatic Doping. *Nature* **2017**, *550* (7677), 487–491.
- (24) Zhang, F.; Zhang, H.; Krylyuk, S.; Milligan, C. A.; Zhu, Y.; Zemlyanov, D. Y.; Bendersky, L. A.; Burton, B. P.; Davydov, A. V.; Appenzeller, J. Electric-Field Induced Structural Transition in Vertical MoTe₂- and Mo_{1-x}W_xTe₂-Based Resistive Memories. *Nat. Mater.* **2019**, *18* (1), 55–61.
- (25) Zhang, K.; Bao, C.; Gu, Q.; Ren, X.; Zhang, H.; Deng, K.; Wu, Y.; Li, Y.; Feng, J.; Zhou, S. Raman Signatures of Inversion Symmetry Breaking and Structural Phase Transition in Type-II Weyl Semimetal MoTe₂. *Nat. Commun.* **2016**, *7* (1), 13552.
- (26) Yang, J.; Colen, J.; Liu, J.; Nguyen, M. C.; Chern, G.; Louca, D. Elastic and Electronic Tuning of Magnetoresistance in MoTe₂. *Sci. Adv.* **2017**, *3* (12), eaao4949.
- (27) Lin, Z.; Liu, Y.; Halim, U.; Ding, M.; Liu, Y.; Wang, Y.; Jia, C.; Chen, P.; Duan, X.; Wang, C.; Song, F.; Li, M.; Wan, C.; Huang, Y.; Duan, X. Solution-Processable 2D Semiconductors for High-Performance Large-Area Electronics. *Nature* **2018**, *562* (7726), 254–258.
- (28) Yu, W.; Dong, Z.; Abdelwahab, I.; Zhao, X.; Shi, J.; Shao, Y.; Li, J.; Hu, X.; Li, R.; Ma, T.; Wang, Z.; Xu, Q.-H.; Tang, D. Y.; Song, Y.; Loh, K. P. High-Yield Exfoliation of Monolayer 1T'-MoTe₂ as Saturable Absorber for Ultrafast Photonics. *ACS Nano* **2021**, *15* (11), 18448–18457.

- (29) Miller, D. A. B.; Chemla, D. S.; Damen, T. C.; Gossard, A. C.; Wiegmann, W.; Wood, T. H.; Burrus, C. A. Band-Edge Electroabsorption in Quantum Well Structures: The Quantum-Confined Stark Effect. *Phys. Rev. Lett.* **1984**, *53* (22), 2173–2176.
- (30) Liu, S.; Fan, X.; Wen, Y.; Liu, P.; Liu, Y.; Pei, J.; Yang, W.; Song, L.; Pan, D.; Zhang, P.; Ma, T.; Lin, Y.; Wang, G.; Hu, G. Conduction Modulation of Solution-Processed 2D Materials. *Adv. Electron. Mater.* **2024**, *10* (6), 2300799.
- (31) Last, G.; Penrose, M. *Lectures on the Poisson Process*; Cambridge University Press: Cambridge, 2017.
- (32) Kingman, J. F. C. *Poisson Processes*; Clarendon Press: Oxford, 1992.
- (33) Dutta, P.; Horn, P. M. Low-Frequency Fluctuations in Solids: 1/f Noise. *Rev. Mod. Phys.* **1981**, *53* (3), 497.
- (34) Van Der Ziel, A. Noise in Solid-State Devices and Lasers. *Proc. IEEE* **1970**, *58* (8), 1178–1206.
- (35) Ma, X.; Liu, Y.-Y.; Zeng, L.; Chen, J.; Wang, R.; Wang, L.-W.; Wu, Y.; Jiang, X. Defects Induced Charge Trapping/Detrapping and Hysteresis Phenomenon in MoS₂ Field-Effect Transistors: Mechanism Revealed by Anharmonic Marcus Charge Transfer Theory. *ACS Appl. Mater. Interfaces* **2022**, *14* (1), 2185–2193.
- (36) Li, L.; Lee, I.; Youn, D.-H.; Kim, G.-H. Hopping Conduction and Random Telegraph Signal in an Exfoliated Multilayer MoS₂ Field-Effect Transistor. *Nanotechnology* **2017**, *28* (7), 075201.
- (37) Kelly, A. G.; O’Suilleabhain, D.; Gabbett, C.; Coleman, J. N. The Electrical Conductivity of Solution-Processed Nanosheet Networks. *Nat. Rev. Mater.* **2021**, *7* (3), 217–234.
- (38) Ashcroft, N. W.; Mermin, N. D. *Solid State Physics*; Cengage Learning: Boston, 2022.

- (39) Martin-Martinez, J.; Diaz, J.; Rodriguez, R.; Nafria, M.; Aymerich, X. New Weighted Time Lag Method for the Analysis of Random Telegraph Signals. *IEEE Electron Device Lett.* **2014**, *35* (4), 479–481.
- (40) Zaman, J.; Ghosh, R. Review on Fifteen Statistical Tests Proposed by NIST. *J. Theor. Phys. Cryptogr.* **2012**, *1*, 18–31.
- (41) Woo, K. S.; Wang, Y.; Kim, Y.; Kim, J.; Kim, W.; Hwang, C. S. A Combination of a Volatile-Memristor-Based True Random-Number Generator and a Nonlinear-Feedback Shift Register for High-Speed Encryption. *Adv. Electron. Mater.* **2020**, *6* (5), 1901117.
- (42) Gutierrez-D, E. A.; Deen, M. J.; Claeys, C. L. *Low Temperature Electronics: Physics, Devices, Circuits, and Applications*; Academic Press: San Diego, 2001.
- (43) Dwork, C. Differential Privacy. In *Automata, Languages and Programming*; Bugliesi, M., Preneel, B., Sassone, V., Wegener, I., Eds.; Springer Berlin Heidelberg: Berlin, Heidelberg, 2006; pp. 1–12.
- (44) He, K.; Zhang, X.; Ren, S.; Sun, J. Deep Residual Learning for Image Recognition. In *2016 IEEE Conference on Computer Vision and Pattern Recognition (CVPR)*, Las Vegas, NV, USA, 2016, pp. 770–778.
- (45) Kvatinsky, S.; Talisveyberg, K.; Fliter, D.; Kolodny, A.; Weiser, U. C.; Friedman, E. G. Models of Memristors for SPICE Simulations. In *2012 IEEE 27th Convention of Electrical and Electronics Engineers in Israel (IEEEI)*, Eilat, Israel, 2012, pp. 1–5.
- (46) Li, Z.; Liu, F.; Yang, W.; Peng, S.; Zhou, J. A Survey of Convolutional Neural Networks: Analysis, Applications, and Prospects. *IEEE Trans. Neural Netw. Learn. Syst.* **2022**, *33* (12), 6999–7019.

Supplementary Notes

Supplementary Note 1: Material production and device fabrication

The raw MoTe₂ powder and other chemicals are purchased from Alpha Aeser and Sigma-Aldrich, and are used as received. The Raw MoTe₂ powder is pressed with high pressure into a solid disk for the electrochemical exfoliation. The electrochemical exfoliation follows the method reported in Ref. (1). For device fabrication, the Au/MoTe₂/Au devices are fabricated on Si/SiO₂, where MoTe₂ is deposited by spin-coating, and the gold electrodes are deposited by electron-beam evaporation. The electron-beam evaporator is IVS EB-600. The MoTe₂ after deposition is baked at 400 °C for 0.5 hours under nitrogen.

Tektronix Keithley 4200-SCS parameter analyzer is used to measure the electrical characteristics of the devices under 300 K at ambient conditions. For the 15 K, 100 K, and 200 K tests, FS-Pro is used under vacuum ($\sim 10^{-6}$ mbar).

Supplementary Note 2: Monte Carlo simulation

Assuming a constant electric field, the change in the polarization of the ferroelectric dipoles will not affect the field, but the internal polarization state of the ferroelectric dipoles in the 1T' MoTe₂ will change. The fluctuation of the polarization can lead to fluctuating bound charges, which can in turn cause fluctuations in the conductance state of the 1T' MoTe₂.

The polarization can switch between two states, i.e. P₁ and P₂, and the switching follows the Arrhenius law². The polarization can thus be modelled as a Poisson process, meaning that the probability of a switch in a small interval of time dt is given by $\lambda * dt$, where λ is the rate of the process. The rate follows the Arrhenius law, given by $\lambda = A * \exp(-E/(k * T))$, where A is the pre-exponential factor, E is the energy barrier, k is the Boltzmann constant, and T is the temperature. However, the switch in polarization now results in fluctuations in the bound charge instead of a change in the electric field. The bound charge ρ_B is related to the polarization P by the relation $\rho_B = -divP$, where div is the divergence operator, indicating that the bound charge is related to the spatial variation of the polarization. In a simple one-dimensional case, this can be described as $\rho_B = -dP/dx$. Now assume that the change in polarization is uniform across the material, the bound charge will change by $\Delta\rho_B$ proportional to the change in polarization ΔP , expressed as $\Delta\rho_B = -\Delta P/L$, where L is a characteristic length scale of the system. This change in voltage can cause a current to flow.

We propose that the change in the bound charge affects the resistance R of the material. A simple model assumes that the resistance is inversely proportional to the absolute value of the bound charge, $R = R_0/\rho_B$, where R_0 is a constant initial resistance. Finally, apply a constant voltage V across this variable resistor, the current I through the material at any time would be given by Ohm's

law, $I(t) = V/R(t)$. The charge from the current can be described by $Q_i = \int_{t=i}^{t=i+1} dI/dt$. So every time the polarization switches, it will change the bound charge, which will then change the resistance and hence, the current fluctuations.

Consider a common effect often found in materials known as Poole-Frenkel behavior³, the current through the material (and hence the resistance) is affected by the applied electric field (which in our case can be linked to the bound charge), and the current density J is given by $J = J_0 * \exp(\beta * \sqrt{\varepsilon})$, where J_0 is the current density at zero field, ε is the electric field, and β is a material constant. In our scenario, we now link the bound charge and the electric field ε . Assume that the change in the bound charge $\Delta\rho_B$ is proportional to the change in electric field $\Delta\varepsilon$, the bound charge is expressed by $\Delta\rho_B = -\Delta\varepsilon/L$. Then, the current density will be dependent on the bound charge. Note that the *sqrt*(ε) means that this is not a simple linear or inversely proportional relationship.

Supplementary Note 3: Neural network recognition

The neural network security is carried out in Python 3 and is based on the ResNet framework. The ResNet variant is based on a ResNet 34 structure, consisting of convolution layers, residual blocks, and so on. The information about the ResNet 34 can be found at: <https://pytorch.org/vision/main/models/generated/torchvision.models.resnet34.html>. The public dataset is from the Visual Geometry Group at the University of Oxford (available at <https://www.robots.ox.ac.uk/~vgg/data/pets/>). The dataset consists of a 37-category pet dataset with roughly 200 images for each class with different scales, poses, and lighting. All the images have an associated ground truth annotation of breed, head ROI, and pixel-level trimap segmentation, and those are used for training and testing.

Supplementary Figures

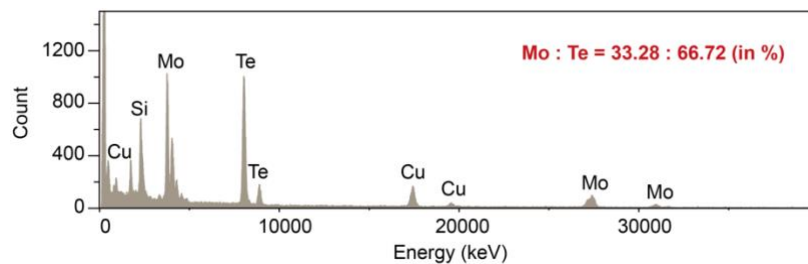


Figure S1. Energy dispersive X-ray spectrometry element mapping of the exfoliated 1T' MoTe₂ nanosheets. The ratio of the Mo and Te atoms is 33.28: 66.72 (in %), proving that there are minimal defects in the exfoliated 1T' MoTe₂ nanosheets.

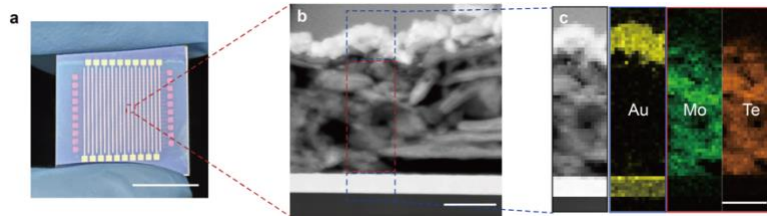


Figure S2. 1T' MoTe₂ device array. (a) Image of an array of 20 ×20 1T' MoTe₂ devices. Spin-coated 1T' MoTe₂ is sandwiched between the evaporated top and bottom gold electrodes to fabricate the devices. The substrate is Si/SiO₂. (b) Cross-sectional scanning electron microscopic image of a typical device, and (c) the corresponding elemental analysis of the selected areas for the Au, Mo, and Te elements, showing clear interfaces between the MoTe₂ layer and the electrodes. Scale bars – (a) 1 cm, (b) 300 nm, and (c) 300 nm.

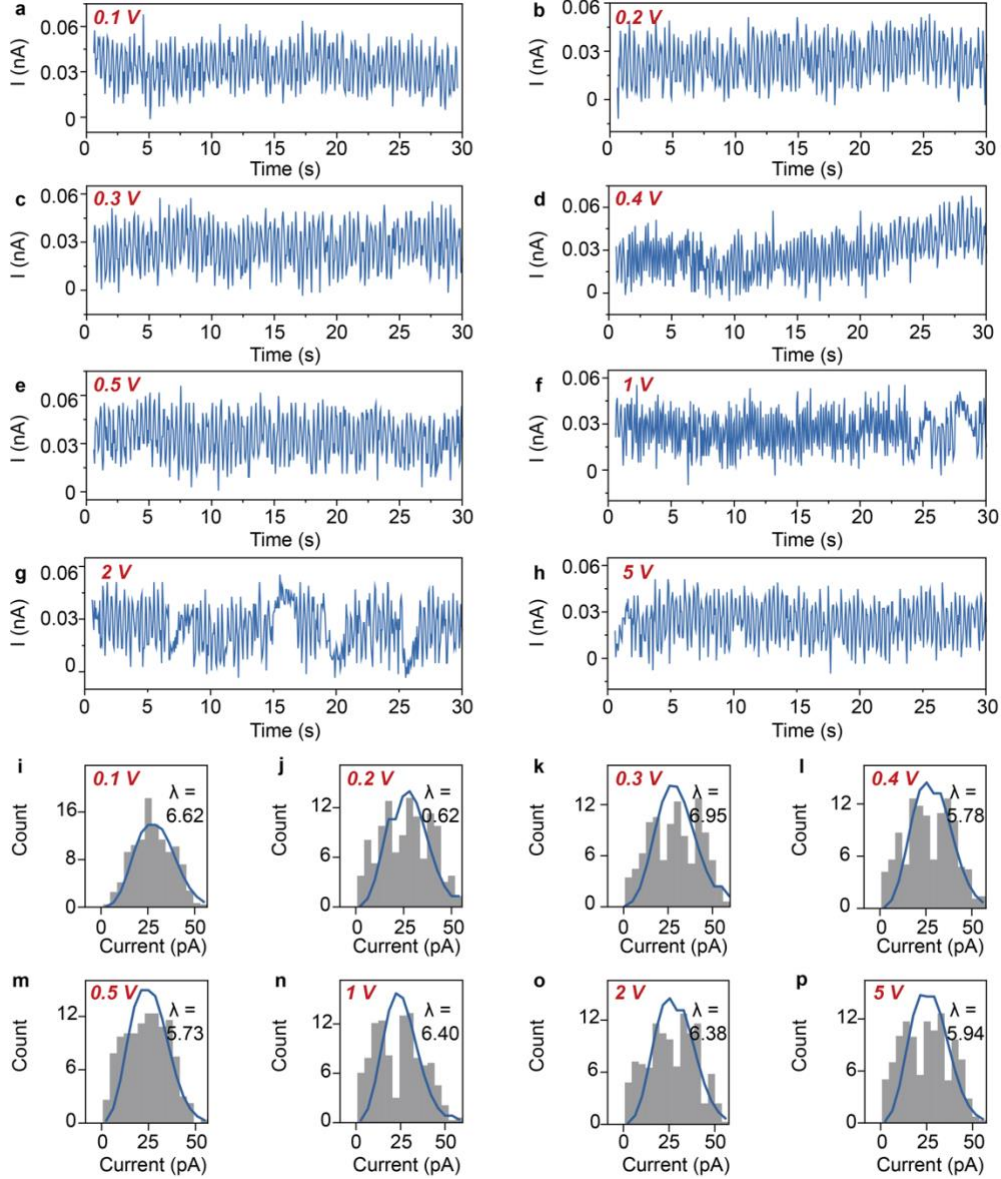


Figure S3. Conductance noise probing at different biases. (a)-(h) Current output of a 1T' MoTe₂ device at bias of 0.1 V, 0.2 V, 0.3 V, 0.4 V, 0.5 V, 1 V, 2 V, and 5 V. The temperature is 300 K. (i)-(p) The corresponding histograms and Poisson fittings of the current data points, proving the conductance noise in the 1T' MoTe₂ device measured at all the bias conditions is a random process and a reliable physical entropy noise.

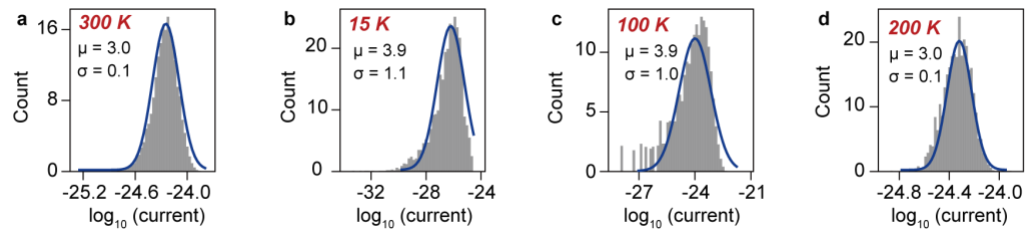


Figure S4. Semi-log-normal distribution of the 1T' MoTe₂ device current output. Histograms and semi-log-normal distribution fittings of the current outputs from Fig. 2b and c.

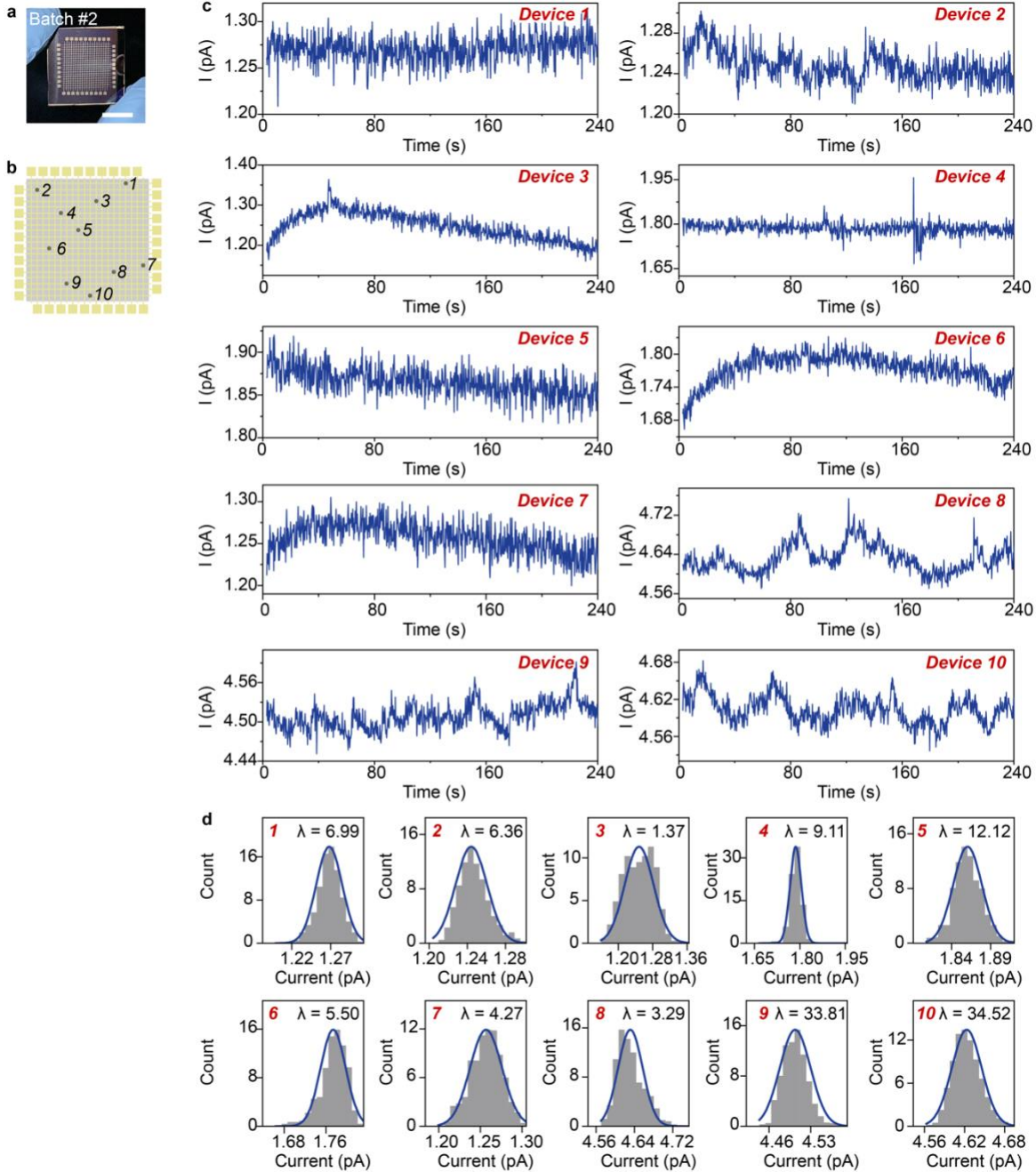


Figure S5. Batch #2 device-to-device conductance noise. (a) 20×20 $1T'$ MoTe_2 devices, with a fabrication yield of $\sim 70\%$, and (b) the corresponding schematic device array showing the working devices randomly selected for the sampling test. (c) Current noise as measured from the selected devices, and (d) the corresponding histograms and Poisson fittings of the current data from (c). Scale bar – (a) 1 cm.

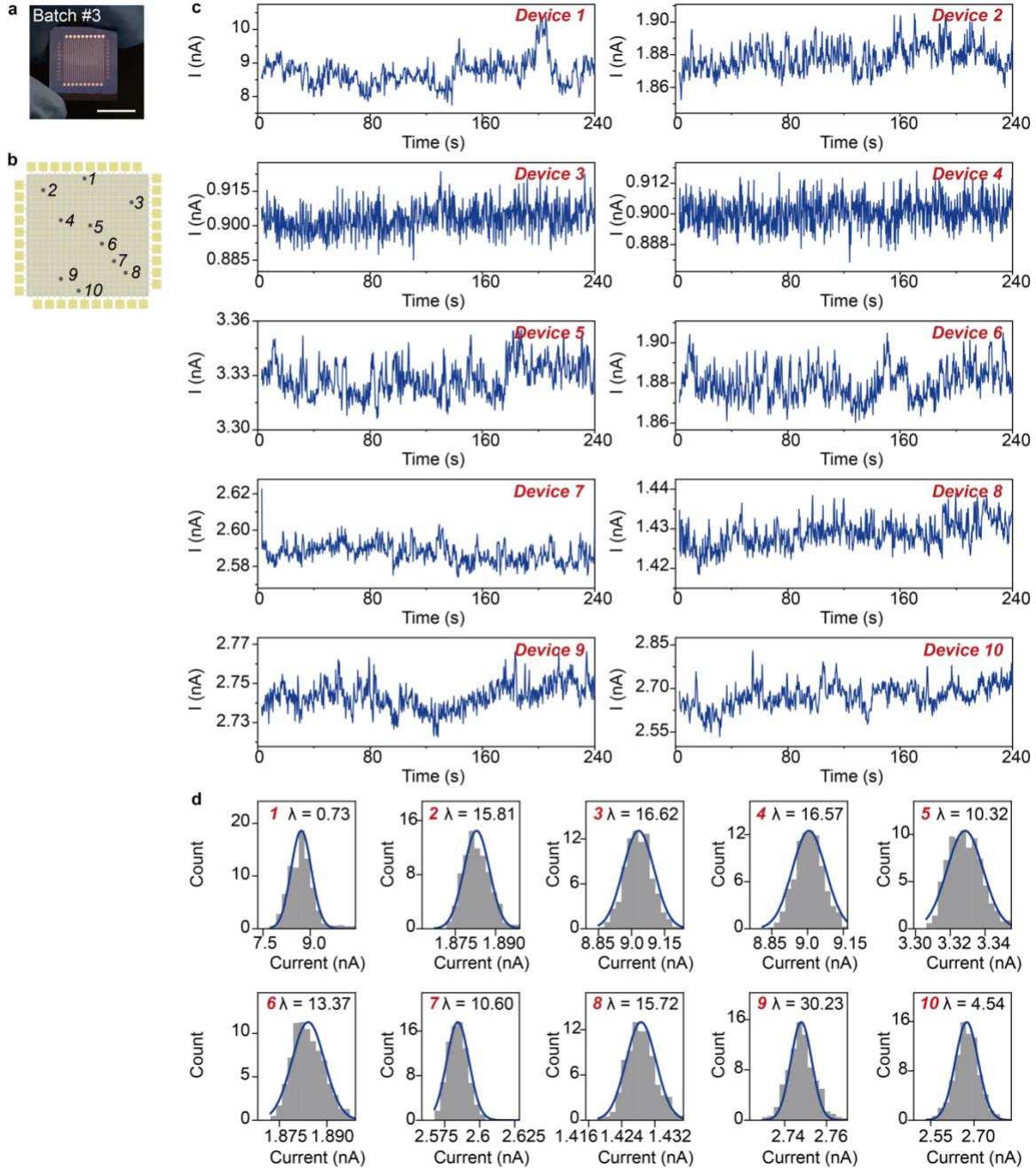


Figure S6. Batch #3 device-to-device conductance noise. (a) 20×20 $1T'$ MoTe_2 devices, with a fabrication yield of $\sim 80\%$, and (b) the corresponding schematic device array showing the working devices randomly selected for the sampling test. (c) Current noise as measured from the selected devices, and (d) the corresponding histograms and Poisson fittings of the current data from (c). Scale bar – (a) 1 cm.

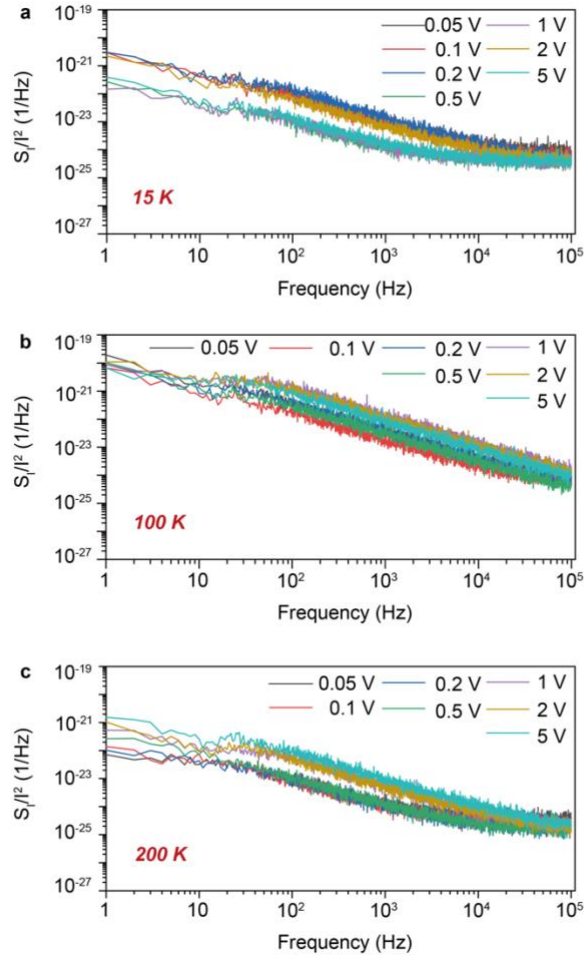


Figure S7. Current power spectral density (PSD) characterization of the 1T' MoTe₂ device at low temperatures. The PSD testing is conducted on the 1T' MoTe₂ device at a low temperature from 15 K to 200 K at the different bias conditions – (a) 15 K, (b) 100 K, and (c) 200 K. The testing proves 1/f noise in the device for all the temperatures and bias testing conditions in the low-frequency region.

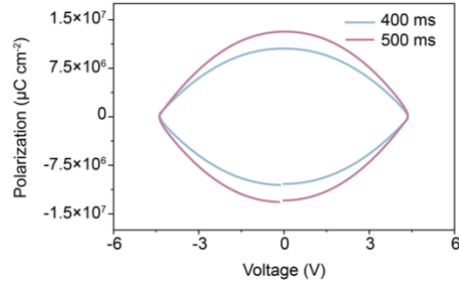


Figure S8. Ferroelectric polarization characterization of the 1T' MoTe₂ device. The ferroelectric polarization testing is conducted on a typical 1T' MoTe₂ device with a sweeping bias, showing no clear evidence of ferroelectric polarization. The test condition: $V_{\text{max}} = 5$ V; Hysteresis speed = 400 ms/500 ms; Preset delay = 1,000 ms. No significant collective polarization is observed in this testing. Further ferroelectric polarization mapping over individual 1T' MoTe₂ nanosheets is required to deterministically locate the exact polarization effect of the ferroelectric dipoles.

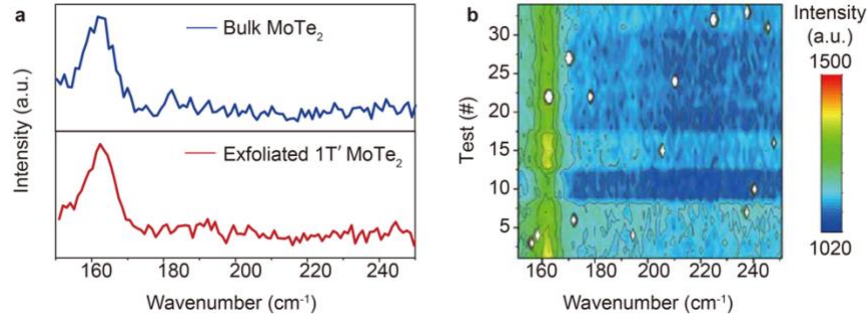


Figure S9. Raman spectroscopy characterization of 1T' MoTe₂. (a) Raman spectrum of bulk and the exfoliated 1T' MoTe₂. (b) Raman spectrum for the same area taken for 35 times. The test condition: wavelength 532 nm, power 2 mW, integration time for a single test 300s, and spot diameter size 1.5 μ m. No deterministic Raman peak shifts can be observed. Two main reasons may account for this – 1) as the spot size is 1.5 μ m in diameter for the Raman spectroscopy characterization, the measured Raman spectrum for the exfoliated 1T' MoTe₂ nanosheets is a collective, averaged Raman spectrum of many 1T' MoTe₂ nanosheets; and 2) each of the Raman spectroscopy tests takes 300 s, and this long time duration is not able to present the variations of the metastable phase structure and ferroelectric polarization. Further Raman spectroscopy on individual 1T' MoTe₂ nanosheets is required to deterministically locate the exact polarization effect of the ferroelectric dipoles.

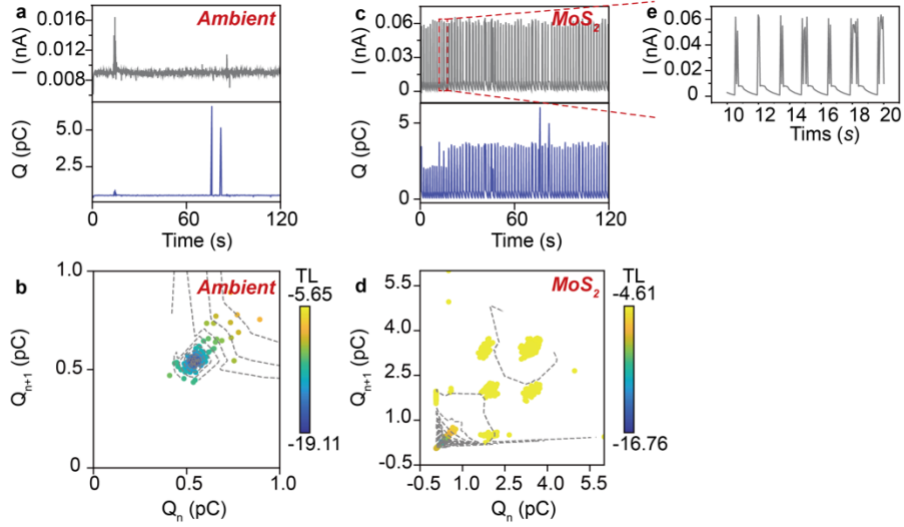


Figure S10. Control experiments of the ambient noise and a MoS₂ device. Current output and the corresponding cumulative charge fluctuations from (a) ambient noise and (c) a MoS₂ device at 0.05 V, 300 K, with (e) showing the detailed current output from the MoS₂ device. Ambient noise is measured by suspending the probing electrodes. MoS₂ is prepared by liquid-phase exfoliation⁴, and is then spin-coated and sandwiched between evaporated top and bottom gold electrodes to fabricate the MoS₂ devices. The device fabrication method and the device configuration are the same as that of the 1T' MoTe₂ devices. The current output of the MoS₂ device shows a distinct random switching behavior, proving random telegraph noise (RTN)⁵ from the MoS₂ device. The origin of the RTN is suggested to be attributed to charge trapping at the defect sites in the MoS₂ material^{6,7}. The cumulative charge is integrated during the sampling time interval of 0.067 s. The time-lag plots for the cumulative charge fluctuations of (b) the ambient noise and (d) the MoS₂ device: the **TL** plot of the ambient noise establishes monostable aggregation with weak correlations in the cumulative charge states, meaning weak correlations in the noise states from the ambient noise; the **TL** plot of the MoS₂ device establishes random aggregation regions with strong correlations in the corresponding cumulative charge states, which may be a result of the charge trapping and de-trapping mechanism.

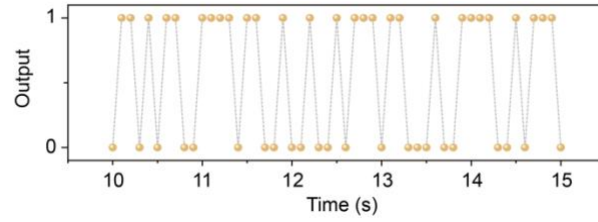


Figure S11. Random bit string of the 0's and 1's true random numbers generated from “port 4” during 10 to 15 seconds (the full-time-scale true random number output is shown in Fig. 4c).

It is shown that the 0's and 1's true random numbers are generated in a random distribution.

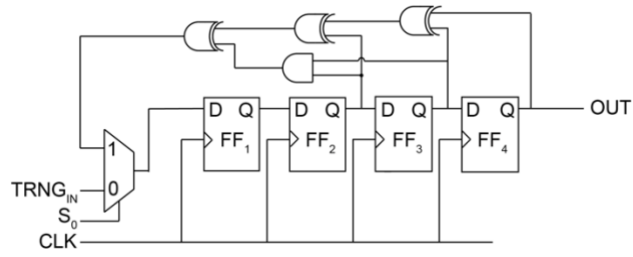


Figure S12. 4-bit nonlinear feedback shift register (NLFSR) circuit design. The NLFSR is used to generate high-throughput random numbers from the seed, i.e. the true random numbers, by setting a high clock frequency, e.g. 1 MHz.

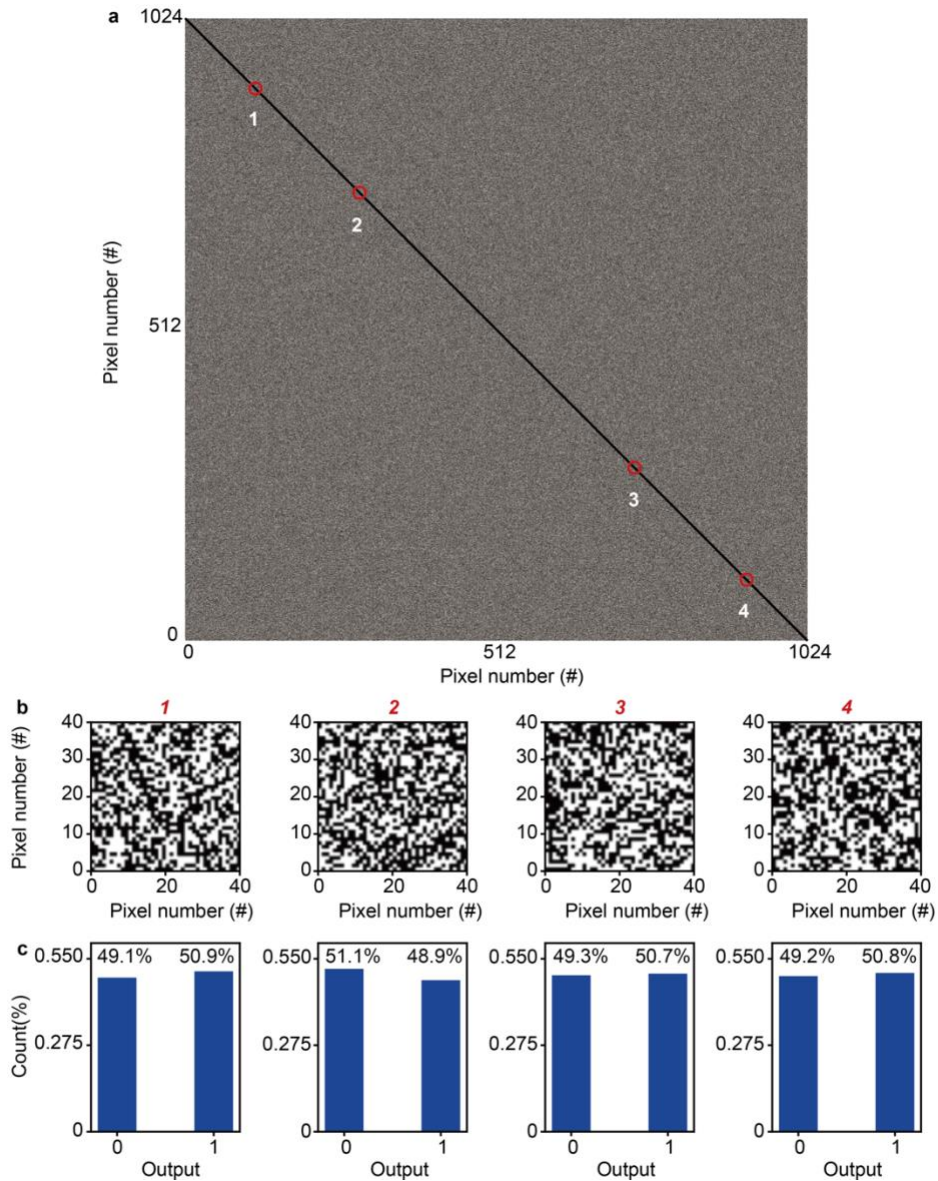


Figure S13. A 1024*1024 bitmap generated using the high-throughput random numbers. To plot the bitmap, the string of the high-throughput random numbers in 0's and 1's digits fills the bitmap sequentially from (0, 0) to (1024, 1024). (a) High-data-volume bitmap. (b) Four randomly selected bitmap regions along the diagonal of the high-data-volume bitmap. (c) The corresponding histograms showing the distributions of the 0's and 1's. The ratios of the 0's and 1's are close to 1 to 1.

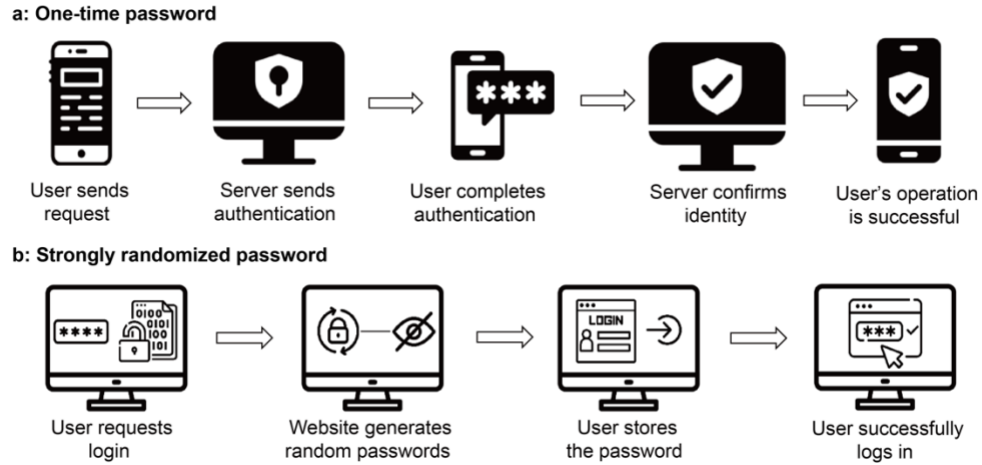


Figure S14. Password generation. (a) Schematic generation and the use of one-time password (OTP) ⁸. OTP is a unique password code that is valid for only one login/transaction session. It is often used as a second factor in two-factor authentication (2FA) and multi-factor authentication (MFA) systems ⁸. (b) Schematic generation and the use of strongly randomized passwords. Strongly randomized passwords can be stored in systems for applications that require a high level of password security.

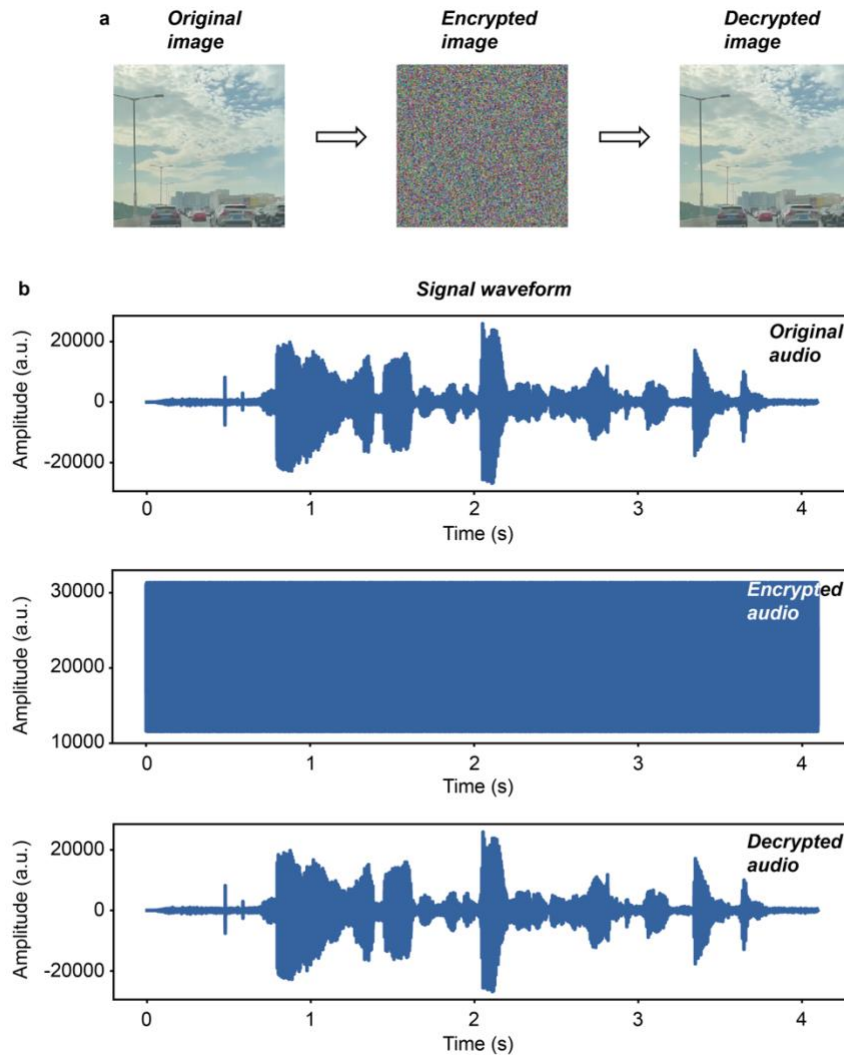


Figure S15. Data encryption. (a) Encryption and decryption of an image. The encryption and decryption are conducted by performing the common encryption/decryption operations (e.g. AES encryption/decryption method ⁹) on the pixels using the high-throughput random numbers generated. (b) Acoustic spectrograms for audio encryption and decryption, showing a four-second audio, the audio after bit-by-bit encryption, and the audio after decryption.

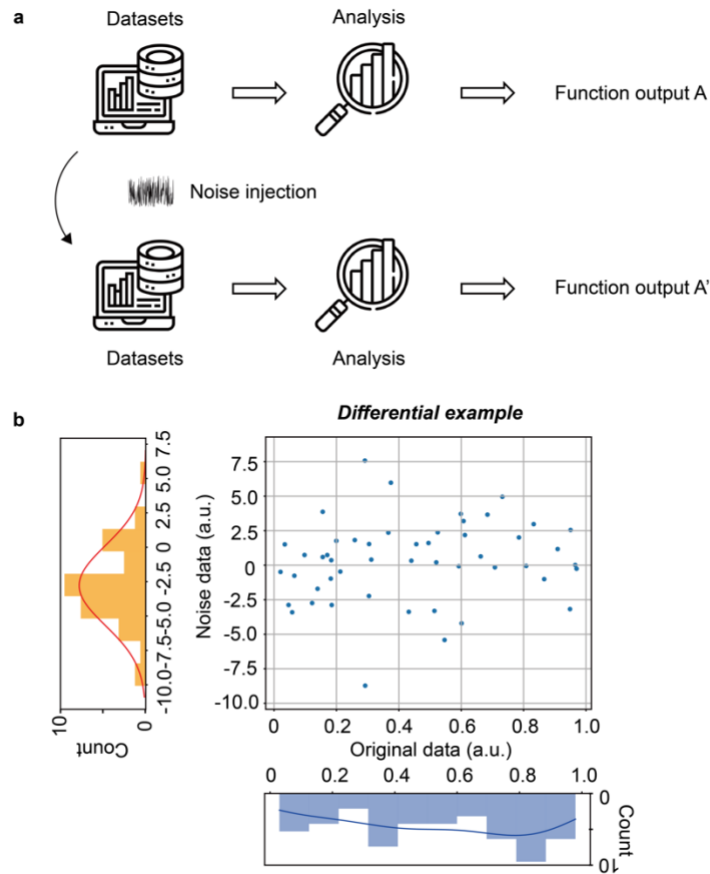


Figure S16. Differential safeguarding strategy. (a) Differential data security workflow. Differential data security is a robust framework used in statistical and machine learning analysis of datasets¹⁰. The core idea is to ensure that the release of the data (or the statistics derived from the data) does not compromise the security of any individuals in the datasets, and that the datasets with the noise perturbation retain the key features. (b) A case example showing injecting noise to a dataset for data security. The left plot shows the noise data, and the bottom plot the original raw data. The noise data is injected into the original data. An example using the differential protection of biometric information such as facial features in neural networks is presented in Fig. 5.

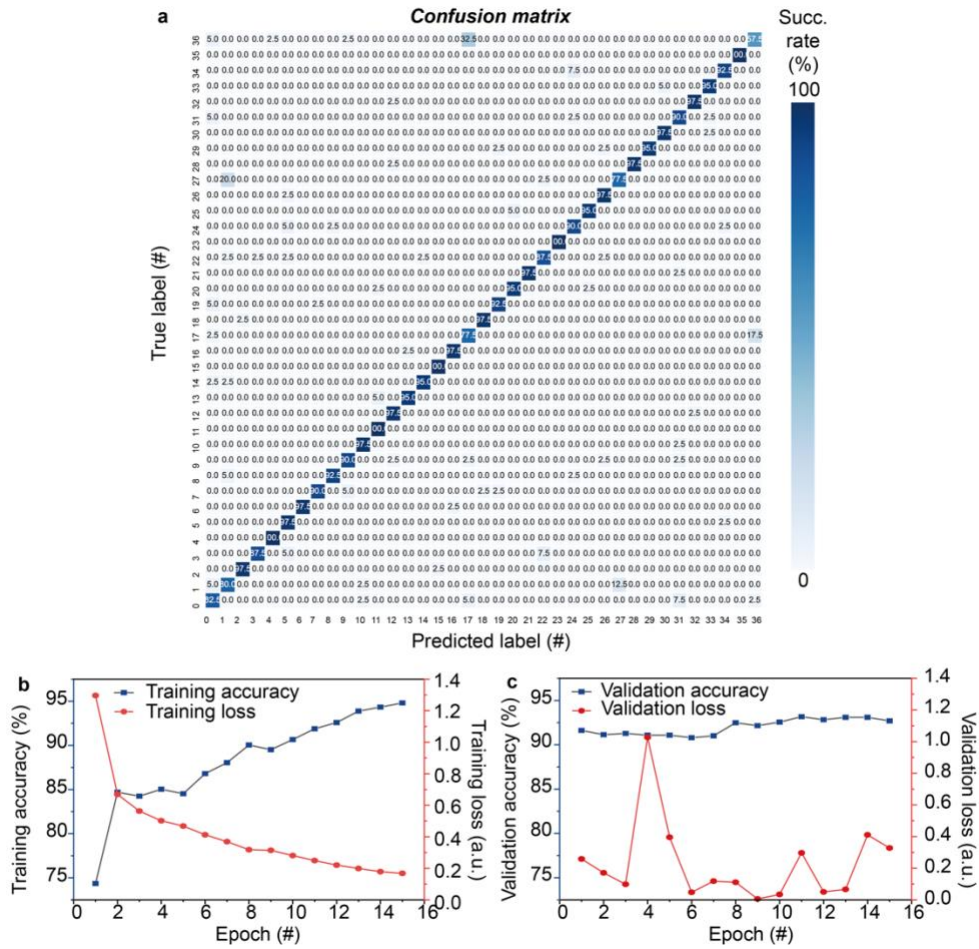


Figure S17. Confusion matrix without noise perturbation and the training performance of the ResNet model. (a) Confusion matrix without noise perturbation. x and y coordinates denote the predicted and true labels of the 37 different classifications in the training dataset, i.e. the Oxford pet-iii dataset. The scale (i.e. the success rate of classification) corresponds to the ratio of the number of the correctly predicted labels to the number of the true labels. The values shown in the confusion matrix represent the success rate, showing the trained ResNet variant achieves a good performance (~92%). (b) The training accuracy and training loss of the ResNet variant. (c) The validation accuracy and validation loss of the ResNet variant. Based on the performance of (b) and (c), it can be concluded that the ResNet variant is well-trained for the Oxford pet-iii dataset.

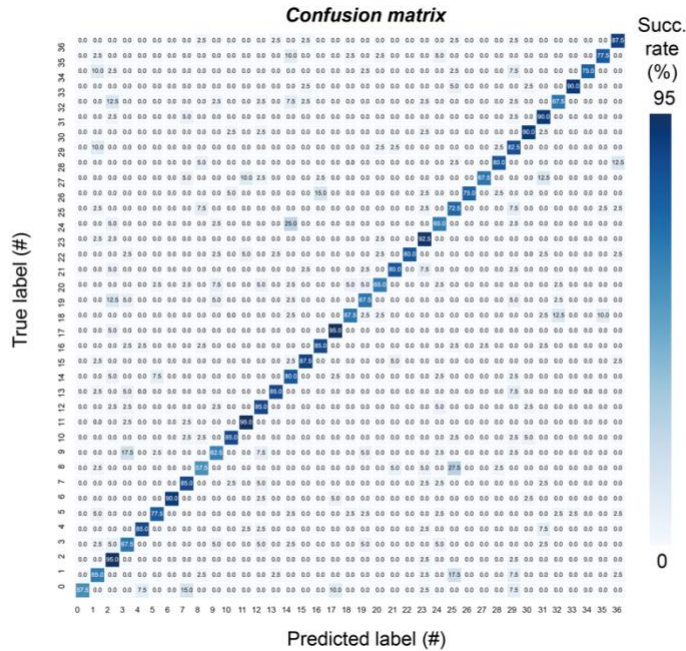


Figure S18. Confusion matrix after noise perturbation, with the success rate values shown.

x and y coordinates denote the predicted and true labels of the 37 different classifications in the training dataset, i.e. the Oxford pet-iii dataset. The scale (i.e. the success rate of classification) corresponds to the ratio of the number of the correctly predicted labels to the number of the true labels. The values shown in the confusion matrix represent the success rate. Comparison with the confusion matrix in Fig. S17a proves that the noise perturbation reduces the accuracy of the ResNet variant model.

Supplementary Tables

Table S1. NIST test of the true random numbers.

	<i>P-value</i>	<i>Success</i>	<i>Post-processing</i>
<i>Approximate entropy</i>	1.0	Success	No
<i>Block frequency</i>	0.824	Success	No
<i>Cumulative sums</i>	0.728, 0.526	Success	No
<i>FFT</i>	0.041	Success	No
<i>Frequency</i>	0.823	Success	No
<i>Linear complexity</i>	-	-	Limited throughput
<i>Longest run</i>	0.445	Success	No
<i>Non-overlapping template</i>	0.999	Success	No
<i>Overlapping template</i>	-	-	Limited throughput
<i>Random excursions</i>	-	Success	No
<i>Random excursions variant</i>	-	Success	No
<i>Rank</i>	-	-	Limited throughput
<i>Runs</i>	0.017	Success	No
<i>Serial</i>	0.499, 0.499	Success	No
<i>Universal</i>	-	-	Limited throughput

Table S2. NIST test of the high-throughput random numbers.

	<i>P-value</i>	<i>Proportion</i>	<i>Success</i>	<i>Post-processing</i>
<i>Approximate entropy</i>	0.409	1	Success	No
<i>Block frequency</i>	0.373	1	Success	No
<i>Cumulative sums</i>	0.047	0.97	Success	No
<i>FFT</i>	0.500	1	Success	No
<i>Frequency</i>	0.057	0.98	Success	No
<i>Linear complexity</i>	0.371	1	Success	No
<i>Longest run</i>	0.965	1	Success	No
<i>Non-overlapping template</i>	0.999	1	Success	No
<i>Overlapping template</i>	0.873	1	Success	No
<i>Random excursions</i>	0.525	1	Success	No
<i>Random excursions variant</i>	0.428	1	Success	No
<i>Rank</i>	0.696	0.99	Success	No
<i>Runs</i>	0.630	1	Success	No
<i>Serial</i>	0.607	1	Success	No
<i>Universal</i>	0.425	1	Success	No

Table S3. Comparison between our random number generator and other reported random number generators.

Material and device	Working principle	Circuit complexity	Integration	Exacting difficulty	Power consumption	Temperature window (K)	Applications	Ref.
Metal/Oxide/Metal memristors	RTN in RRAM	Moderate	high	Moderate	0.18-18,900 nW	295.15	TRNG	11
Pt/Ag/Ag:SiO ₂ /Pt	Stochastic switching in RRAM	Low	high	Easy	/	295.15-358.15	TRNG	12
Pt/Ti/NbO _x /Pt	Stochastic oscillation in RRAM	Moderate	high	Easy	/	300-390	TRNG	13
Silicon-based MTJ	Stochastic switching time in MRAM	High	Moderate	Difficult	18 pJ/bit	248-373.15	TRNG	14
MTJ	Stochastic magnetization in MRAM	/	Moderate	Difficult	/	300	TRNG	15
MTJ with CNTFET	Stochastic behavior in MRAM	High	Moderate	Difficult	1.11 pJ/bit	300	TRNG	16
Silicon-based FeFET	Process variations and ferroelectric-material degradation in FeRAM	High	Moderate	Moderate	/	300	TRNG	17
TiN/HfO ₂ /SiON FeFET	Stochastic switching in FeRAM	Low	Moderate	Moderate	/	/	TRNG	18

Straintronic GFET	Strain-induced reversible cracking	/	/	Easy	/	298.15	PUF	19
MoS ₂ FET	Inherent stochasticity in the voltage transfer	Low	Moderate	Easy	30 pJ/bit	298.15-373.15	TRNG	20
MoS ₂ memtransistor	D2D variation	/	/	Easy	/	298.15	PUF	21
TMO/TMD camouflaged resistors	the properties of TMDs and transition-metal oxides	/	/	Easy	/	/	Hardware obfuscation	22
MoS ₂ memtransistor	Programming stochasticity	Low	/	Easy	<1 nJ	/	Stochastic computing	23
GFET	D2D variation	/	/	Easy	/	100-380	PUF	24
hBN memristor	RTN in RRAM	Moderate	high	Easy	/	295.15-423.15	TRNG	25
This work	Polarization variation	Low	High	Easy	50 nW	15-300	TRNG	/

Note the power consumption in this table considers the consumption from the functional device only. (MTJ: magnetic tunnel junction; CNTFET: carbon nanotube field-effect transistor; FeFET: ferroelectric field-effect transistor; GFET: graphene field-effect transistor; FET: field-effect transistor; TMO/TMD: transition metal oxide/transition metal dichalcogenide; RTN: random telegraph noise; RRAM: resistive random-access memory; MRAM: magnetoresistive random-access memory; FeRAM: ferroelectric random-access memory; D2D: device-to-device; TRNG: true random number generator; PUF: physical unclonable function.)

Supplementary References

- (1) Yu, W.; Dong, Z.; Abdelwahab, I.; Zhao, X.; Shi, J.; Shao, Y.; Li, J.; Hu, X.; Li, R.; Ma, T.; Wang, Z.; Xu, Q.-H.; Tang, D. Y.; Song, Y.; Loh, K. P. High-Yield Exfoliation of Monolayer 1T'-MoTe₂ as Saturable Absorber for Ultrafast Photonics. *ACS Nano* **2021**, *15* (11), 18448–18457.
- (2) Modine, F. A.; Major, R. W.; Choi, S. I.; Bergman, L. B.; Silver, M. N. Polarization Currents in Varistors. *J. Appl. Phys.* **1990**, *68* (1), 339–346.
- (3) Hartke, J. L. The Three-dimensional Poole-Frenkel Effect. *J. Appl. Phys.* **1968**, *39* (10), 4871–4873.
- (4) Hu, G.; Yang, L.; Yang, Z.; Wang, Y.; Jin, X.; Dai, J.; Wu, Q.; Liu, S.; Zhu, X.; Wang, X.; Wu, T.-C.; Howe, R. C. T.; Albrow-Owen, T.; Ng, L. W. T.; Yang, Q.; Occhipinti, L. G.; Woodward, R. I.; Kelleher, E. J. R.; Sun, Z.; Huang, X.; Zhang, M.; Bain, C. D.; Hasan, T. A General Ink Formulation of 2D Crystals for Wafer-Scale Inkjet Printing. *Sci. Adv.* **2020**, *6* (33), eaba5029.
- (5) Kogan, S. Random Telegraph Noise in Microstructures. *Phys. Rev. Lett.* **1998**, *81* (14), 2986.
- (6) Song, S. H.; Joo, M.-K.; Neumann, M.; Kim, H.; Lee, Y. H. Probing Defect Dynamics in Monolayer MoS₂ via Noise Nanospectroscopy. *Nat. Commun.* **2017**, *8* (1), 2121.
- (7) Ma, X.; Liu, Y.-Y.; Zeng, L.; Chen, J.; Wang, R.; Wang, L.-W.; Wu, Y.; Jiang, X. Defects Induced Charge Trapping/Detrapping and Hysteresis Phenomenon in MoS₂ Field-Effect Transistors: Mechanism Revealed by Anharmonic Marcus Charge Transfer Theory. *ACS Appl. Mater. Interfaces* **2022**, *14* (1), 2185–2193.
- (8) Ometov, A.; Bezzateev, S.; Mäkitalo, N.; Andreev, S.; Mikkonen, T.; Koucheryavy, Y. Multi-Factor Authentication: A Survey. *Cryptography* **2018**, *2* (1), 1.

- (9) National Institute of Standards and Technology (NIST); Dworkin, M. J.; Barker, E.; Nechvatal, J.; Fotti, J.; Bassham, L. E.; Roback, E.; Dray, J. Advanced Encryption Standard (AES); Federal Inf. Process. Stds. (NIST FIPS), 2001, 197.
- (10) Dwork, C. Differential Privacy. In *Automata, Languages and Programming*; Bugliesi, M., Preneel, B., Sassone, V., Wegener, I., Eds.; Springer Berlin Heidelberg: Berlin, Heidelberg, 2006; pp. 1–12.
- (11) Li, X.; Zanotti, T.; Wang, T.; Zhu, K.; Puglisi, F. M.; Lanza, M. Random Telegraph Noise in Metal-Oxide Memristors for True Random Number Generators: A Materials Study. *Adv. Funct. Mater.* **2021**, *31* (27), 2102172.
- (12) Jiang, H.; Belkin, D.; Savel'ev, S. E.; Lin, S.; Wang, Z.; Li, Y.; Joshi, S.; Midya, R.; Li, C.; Rao, M.; Barnell, M.; Wu, Q.; Yang, J. J.; Xia, Q. A Novel True Random Number Generator Based on a Stochastic Diffusive Memristor. *Nat. Commun.* **2017**, *8* (1), 882.
- (13) Kim, G.; In, J. H.; Kim, Y. S.; Rhee, H.; Park, W.; Song, H.; Park, J.; Kim, K. M. Self-Clocking Fast and Variation Tolerant True Random Number Generator Based on a Stochastic Mott Memristor. *Nat. Commun.* **2021**, *12* (1), 2906.
- (14) Yang, K.; Dong, Q.; Wang, Z.; Shih, Y.-C.; Chih, Y.-D.; Chang, J.; Blaauw, D.; Svlvester, D. A 28NM Integrated True Random Number Generator Harvesting Entropy from MRAM. *2018 IEEE Symposium on VLSI Circuits (VLSIC)*, Honolulu, HI, USA, 2018, pp. 171–172.
- (15) Chen, X.; Zhang, J.; Xiao, J. Magnetic-Tunnel-Junction-Based True Random-Number Generator with Enhanced Generation Rate. *Phys. Rev. Appl.* **2022**, *18* (2), L021002.
- (16) Amirany, A.; Jafari, K.; Moaiyeri, M. H. True Random Number Generator for Reliable Hardware Security Modules Based on a Neuromorphic Variation-Tolerant Spintronic Structure. *IEEE Trans. Nanotechnol.* **2020**, *19*, 784–791.

- (17) Siu, J. W. K.; Eslami, Y.; Sheikholeslami, A.; Gulak, P. G.; Endo, T.; Kawashima, S. A Current-Based Reference-Generation Scheme for 1T-1C Ferroelectric Random-Access Memories. *IEEE J. Solid-State Circuits* **2003**, *38* (3), 541–549.
- (18) Mulaosmanovic, H.; Mikolajick, T.; Slesazeck, S. Random Number Generation Based on Ferroelectric Switching. *IEEE Electron Device Lett.* **2017**, *39* (1), 135–138.
- (19) Ghosh, S.; Zheng, Y.; Radhakrishnan, S. S.; Schranghamer, T. F.; Das, S. A Graphene-Based Straintronic Physically Unclonable Function. *Nano Lett.* **2023**, *23* (11), 5171–5179.
- (20) Ravichandran, H.; Sen, D.; Wali, A.; Schranghamer, T. F.; Trainor, N.; Redwing, J. M.; Ray, B.; Das, S. A Peripheral-Free True Random Number Generator Based on Integrated Circuits Enabled by Atomically Thin Two-Dimensional Materials. *ACS Nano* **2023**, *17* (17), 16817–16826.
- (21) Oberoi, A.; Dodda, A.; Liu, H.; Terrones, M.; Das, S. Secure Electronics Enabled by Atomically Thin and Photosensitive Two-Dimensional Memtransistors. *ACS Nano* **2021**, *15* (12), 19815–19827.
- (22) Wali, A.; Ravichandran, H.; Das, S. A Machine Learning Attack Resilient True Random Number Generator Based on Stochastic Programming of Atomically Thin Transistors. *ACS Nano* **2021**, *15* (11), 17804–17812.
- (23) Ravichandran, H.; Zheng, Y.; Schranghamer, T. F.; Trainor, N.; Redwing, J. M.; Das, S. A Monolithic Stochastic Computing Architecture for Energy Efficient Arithmetic. *Adv. Mater.* **2023**, *35* (2), 2206168.
- (24) Dodda, A.; Subbulakshmi Radhakrishnan, S.; Schranghamer, T. F.; Buzzell, D.; Sengupta, P.; Das, S. Graphene-Based Physically Unclonable Functions That Are Reconfigurable and Resilient to Machine Learning Attacks. *Nat. Electron.* **2021**, *4* (5), 364–374.

(25) Wen, C.; Li, X.; Zanotti, T.; Puglisi, F. M.; Shi, Y.; Saiz, F.; Antidormi, A.; Roche, S.; Zheng, W.; Liang, X.; Hu, J.; Duhm, S.; Roldan, J. B.; Wu, T.; Chen, V.; Pop, E.; Garrido, B.; Zhu, K.; Hui, F.; Lanza, M. Advanced Data Encryption Using 2D Materials. *Adv. Mater.* **2021**, *33* (27), 2100185.